

NO EVIDENCE FOR THE AQUARIUS CO-MOVING GROUP RESULTING FROM A DISRUPTED CLASSICAL GLOBULAR CLUSTER¹

ANDREW R. CASEY^{2,3}, STEFAN KELLER², ALAN ALVES-BRITO², ANNA FREBEL³, GARY DA COSTA², AMANDA KARAKAS²,
DAVID YONG², KEVIN SCHALUFMAN³, HEATHER JACOBSON³, QINQIN YU³, KEN FREEMAN², CHERIE FISHLOCK²

Draft version May 7, 2013

ABSTRACT

We present a detailed analysis of high S/N, high-resolution spectra for five Aquarius stream stars observed using the MIKE spectrograph on the Magellan Clay telescope. Our sample represents one third of the total number of published stream members. We find the co-moving group is not chemically coherent; a wide metallicity dispersion ranging from $[Fe/H] = -0.63$ to -1.63 dex is observed. Enhanced $[Na/Fe]$, $[Ni/Fe]$ and $[\alpha/Fe]$ abundance ratios suggest the co-moving group is not the result of a disrupted dwarf galaxy. Additionally, we find no evidence that the stream is a result of a disrupted classical globular cluster, contrary to a previously published claim. No inverse Na-O correlation is present, and we find a strong positive Mg-Al relationship similar to that observed in the thick disc. The group is chemically indistinguishable from Milky Way field stars with the exception of one candidate, C222531-145437. From positions, velocities, and detailed chemical abundances it is unambiguous that C222531-145437 is a tidal remnant from the ω -Centauri globular cluster. We hypothesise the co-moving group is galactic in origin, and is a result from a disc-satellite perturbation in the Milky Way thick disc. Derived orbits, $u-v$ plane velocities, and angular momentum calculations for Aquarius candidates qualitatively supports our hypothesis, and are consistent with a disc interaction on the order of a few Gyr ago. Given the debris of C222531-145437 as tidal debris, ω -Centauri is a plausible perturber, as is the Sagittarius dwarf. While there is no evidence that the Aquarius stream is the tidal tail of a disrupted satellite, we advocate the ‘Aquarius group’ as a more appropriate description. Like the Canis Major over-density, and the Hercules and Monoceros groups, the Aquarius co-moving group adds to the list of kinematically-identified substructures that are not actually accreted material; they are simply part of the rich complexity of the Milky Way structure.

Subject headings: Galaxy: halo, structure

1. INTRODUCTION

Galaxies are hierarchically formed through chaotic mergers of smaller systems. The Milky Way is no exception. The accumulating stellar debris in our own galactic halo provides ongoing evidence for such merging events. As accreting satellites infall onto the galaxy, tidal forces disrupt the smaller system, hurtling stars in leading and trailing directions. Unsurprisingly the velocities of stars within these ‘stellar streams’ are sensitive to the galactic potential. As such, their phase-space information can collectively constrain the fraction and distribution of accreted matter in the galaxy, the sub-halo mass function, as well as the shape and extent of dark matter in the Milky Way. Moreover, individual chemical abundances from high-resolution spectra can trace the chemical evolution of the galaxy.

Wide-field deep imaging surveys have proved excellent sources for finding stellar streams. Dozens have been identified through careful photometric selections and matched-filtering techniques, with some to a galactocentric distance of 100 kpc (Belokurov et al. 2007; Drake et al. 2013). Indeed, it is clear that a large fraction of

the stellar halo has been built up by accretion. However, as Helmi & White (1999) point out, these detection strategies are only successful for identifying streams that are sufficiently distant from the solar neighbourhood. A nearby stream, within ~ 10 kpc, will not appear as a photometric over-density as the stars would be sparsely positioned across the sky. Such substructures would only be detectable by their kinematics, or perhaps with precise elemental abundances through a ‘chemical tagging’ approach (e.g. see Freeman & Bland-Hawthorn (2002)).

It is therefore necessary to spectroscopically survey the solar neighbourhood stars to reveal any nearby substructures. The Radial Velocity Experiment (RAVE) team began such a survey in 2003 and have observed spectra from over 500,000 stars across $17,000$ deg². As the name hints, the primary goal of RAVE was to obtain radial velocities for the solar neighbourhood and beyond. In an attempt to remain kinematically unbiased, RAVE candidates were selected solely by their apparent magnitude. With the exception of bulge stars, where some photometric cuts were employed, all stars between $9 < I < 13$ were observed. Almost all of these candidates have published radial velocity measurements (Steinmetz et al. 2006), and for a subset of stars with a sufficient Signal-to-Noise (S/N) ratio, estimates of stellar parameters have been derived using a χ^2 minimisation technique (Zwitter et al. 2008; Siebert et al. 2011).

Using these data, Williams et al. (2011) identified a co-moving group of nearby ($0.5 \text{ kpc} \lesssim d \lesssim 10 \text{ kpc}$)

¹ This paper includes data gathered with the 6.5 meter Magellan Telescopes located at Las Campanas Observatory, Chile.

² Research School of Astronomy & Astrophysics, Australian National University, Mount Stromlo Observatory, via Cotter Rd, Weston, ACT 2611, Australia; acasey@mso.anu.edu.au

³ Massachusetts Institute of Technology, Kavli Institute for Astrophysics and Space Research, 77 Massachusetts Avenue, Cambridge, MA 02139, USA

stars in the vicinity of the Aquarius constellation ($l, b = (60^\circ, -55^\circ)$). Thus, the co-moving group was named the Aquarius stream. The group is most apparent when examining velocities against galactic latitude for stars within $-70^\circ < b < -50^\circ$. Williams et al. (2011) employed a selection criteria of $-250 \text{ km s}^{-1} < V_{\text{hel}} < -150 \text{ km s}^{-1}$, $30^\circ < l < 75^\circ$ and $J > 10.3$ to maximize the contrast between the stream and background, identifying 15 candidates in the process. The average heliocentric velocity of these members was found to be $V_{\text{hel}} = -199 \text{ km s}^{-1}$, with a dispersion of 27 km s^{-1} . The radial velocity uncertainties provided by the RAVE catalog are described to be $\sim 2 \text{ km s}^{-1}$, so the stream's wide kinematic distribution appears to be real.

Upon examining the galactic longitude and velocities of Aquarius stars, the stream appears quite distinct from the halo. In order to quantify the statistical likelihood that the Aquarius stream is truly separate from a smooth halo distribution, Williams et al. (2011) compared the number of observed RAVE stars within $-70^\circ < b < -50^\circ$ against the Galaxia (Sharma et al. 2011) and Besançon (Robin et al. 2003) galaxy simulations. The predicted particles in each model between $-70^\circ < b < -50^\circ$ were binned in $\Delta l \times \Delta V_{\text{hel}}$ blocks using varying grid cell sizes between 25° to 70° and 20 km s^{-1} to 100 km s^{-1} . The RAVE sample was binned in the same way, discretising the inferred statistical significance of the observed over-density. Williams et al. (2011) found the stream to be significant ($> 4\sigma$) in 96% of the cell proportions employed for the Besançon model. By sampling the Galaxia model repeatedly with varying extinction rates, a similar result was found: between $75 \pm 15\%$ to $80 \pm 18\%$ of grid cells showed the Aquarius stream to be significant at the 4σ level or higher. Given the high-latitude and proximity of the stream, it is not surprising that dust had a negligible effect on the statistical significance. Williams et al. (2011) concluded that the over-density in l, V_{hel} is a true substructure, and neither the choice of galaxy model, cell dimension, nor the extinction rate made any real difference to the detection significance.

The Sagittarius stream is arguably the most prominent ongoing accretion event in the galaxy. Given the extent of stellar debris the Sagittarius dwarf spheroidal (dSph) galaxy has littered throughout the Milky Way, it is reasonable to suspect the Aquarius stream might originate from the Sagittarius dwarf. Indeed, the Aquarius stars do not lie far from the orbital plane of Sagittarius and the metallicities reported by Williams et al. (2011) are not dissimilar from the Sagittarius stream. However, Williams et al. (2011) found the Aquarius transverse motions (specifically V_Z and V_ϕ) to be quite distinct from Sagittarius. Based on the phase space information available, Williams et al. (2011) concluded that the newly discovered stream could not be positively associated with the Monoceros stream, Hercules-Aquila cloud, or either the Canis Major or Virgo over-densities.

RAVE observations suggest the Aquarius stream has a metallicity of $[\text{Fe}/\text{H}] \sim -1.0$, slightly more metal-rich than halo stars at the same distance. Using stellar parameters from the RAVE pipeline, Williams et al. (2011) found the stream to have an average of $[\text{M}/\text{H}] = -1.0 \pm 0.4 \text{ dex}$, compared to

$[\text{M}/\text{H}] = -1.1 \pm 0.6 \text{ dex}$ for background stars after the same selection cuts had been employed. Of the 15 Aquarius stars in the Williams et al. (2011) discovery sample with stellar parameters, the metallicity range from medium-resolution spectroscopy is wide: between -2.02 and -0.33 dex . High-resolution spectroscopic observations with high S/N are necessary to accurately characterise the stream's metallicity distribution.

To this end, Wylie-de Boer et al. (2012) obtained high-resolution ($\mathcal{R} = 25,000$) spectra with modest S/N ($\sim 30 \text{ pixel}^{-1}$) for six Aquarius stream stars using the echelle spectrograph on the ANU 2.3m telescope. Their data indicate a surprisingly narrow metallicity distribution compared to the RAVE results: $[\text{Fe}/\text{H}] = -1.09 \pm 0.10 \text{ dex}$ extending from $[\text{Fe}/\text{H}] = -1.25$ to -0.98 dex . Observations of such minimal chemical scatter from stars that share a common origin is typically noted only in either globular or open clusters. The largest $[\text{Fe}/\text{H}]$ discrepancy between the Williams et al. (2011) and Wylie-de Boer et al. (2012) study was $\Delta[\text{Fe}/\text{H}] = -0.66 \text{ dex}$ for the most metal-rich star in the Williams et al. (2011) sample. The most metal-poor star in the Williams et al. (2011) study was not observed by Wylie-de Boer et al. (2012).

In addition to ascertaining stellar parameters, Wylie-de Boer et al. (2012) measured elemental abundances for the Aquarius stream stars – the only study to do so until now. The authors primarily focussed on light elements: Na, O, Ni, Mg, and Al. Chemical patterns in these elements arise as natural consequences of nucleosynthetic processes in massive stars and have been repeatedly observed in globular clusters. Specifically, an anti-correlation between sodium and oxygen content appears ubiquitous to globular cluster stars. While the exact formation mechanism is still under debate, the chemical relationship is well-established empirically. The Na-O pattern provides the best chemical evidence that their enrichment history has been dominated by Type II supernova (SN) events, and that those stars formed in a globular cluster-like environment.

From high-resolution spectroscopy of six Aquarius stars, four of which have sodium and oxygen abundance measurements, Wylie-de Boer et al. (2012) found two stars with enhanced sodium; slightly higher $[\text{Na}/\text{Fe}]$ ratios than halo stars of the same metallicity. However, no strong oxygen depletion was evident in the data. Thus, although they found minimal chemical scatter in the overall metallicities of Aquarius stream stars, they observed no evidence of a Na-O inverse correlation.

There are other chemical abundance patterns that allow us to infer the stream's chemical enrichment environment. Nissen & Schuster (1997) first noted that nearby solar neighbourhood stars were enriched in $[\text{Ni}/\text{Fe}]$ and $[\text{Na}/\text{Fe}]$. Fulbright (2000) came to a similar conclusion: only somewhat distant ($R_\odot > 20 \text{ kpc}$) stars are likely to be sodium deficient. If the stellar halo has been built up from the accretion of smaller dwarf satellites, Nissen & Schuster (1997) proposed that this chemical trend may be indicative of the halo merger history since stars at larger R_\odot are more likely to have been accreted rather than formed in-situ. Wylie-de Boer et al. (2012) found all the Aquarius stars in their sample to be enriched in both sodium and nickel; contrary to what would be expected

if the stars originated from a disrupted dSph galaxy. If the stream had originated from an accretion event, this provides an indication that the stars were first enriched in a globular cluster-like environment.

Combined with the low level of chemical scatter present in their sample, these chemical indicators led Wylie-de Boer et al. (2012) to conclude that the Aquarius stream is the result of a tidally disrupted globular cluster. Williams et al. (2011) had previously precluded this possibility with any known clusters after modelling an Aquarius-like progenitor infalling onto the Milky Way and comparing the predicted l, b, V_{hel} with known, nearby globular clusters of similar metallicities. No known globular cluster could match their simulation. If both scenarios are accurate then the undiscovered disrupting cluster might still remain and would be very close, such that it is unlikely it would not have been discovered by now.

We seek to investigate the nature of the Aquarius stream, specifically the recent globular cluster origin claim made by Wylie-de Boer et al. (2012). We present a detailed analysis for five Aquarius stream candidates from high-resolution, high S/N observations taken using the Magellan Inamori Kyocera Echelle spectrograph (Bernstein et al. 2003) with the Magellan Clay telescope. Details of the observations and data reduction are outlined in the following section. The data analysis is chronicled in Section 3 and a detailed discussion of these results resides in Section 4. In Section 5 we present a summary of our conclusions and critical interpretations.

2. OBSERVATIONS & DATA REDUCTION

The most complete sample of Aquarius stream stars is presented in the discovery paper of Williams et al. (2011). Our sample includes five stars: four common to the Wylie-de Boer et al. (2012) study, and an additional candidate from the original Williams et al. (2011) sample. The supplementary star, C2306265-085103, was observed by the RAVE survey but had a S/N ratio too low for stellar parameters to be accurately determined. All program stars were observed in July 2011 in reasonable seeing at low airmass (Table 1), and six standard stars were observed in March 2011. All observations were taken using a $1.0''$ slit, providing a spectral resolution in excess of $\mathcal{R} = 28,000$ in the blue arm and $\mathcal{R} = 22,000$ in the red arm. The exposure time for our program stars was 650 seconds per star in order to ensure a S/N ratio in excess of 100 pixel^{-1} at 600 nm .

Calibration frames were taken at the start of each night, including twenty flat-field frames (10 quartz, 10 milky) and 10 Th-Ar arc lamp exposures for wavelength calibration. The data were reduced using the CarPy pipeline⁴. One standard star, HD 41667, was also reduced using standard extraction and calibration methods in IRAF. The resultant spectra from both approaches were compared for residual fringing, S/N , and wavelength calibration. No noteworthy differences were present, and the CarPy pipeline was utilised for the remainder of the data reduction. Each reduced echelle order was carefully normalised using a third order spline with defined knot spacing. Normalised orders were stitched together to provide a single one-dimensional spectrum from 333-916 nm.

⁴ <http://code.obs.carnegiescience.edu/mike>

The white dwarf HR 6141 was observed in March 2011 as a telluric standard. The S/N ratio for HR 6141 exceeds that in any of our standard or program stars. Although the atmospheric conditions at Las Campanas Observatory are certain to change throughout the night and between observing runs, we are primarily using this spectra to identify stellar absorption lines that are affected by telluric absorption. However, a few critical transitions necessary for abundance analyses that are affected by the Earth's atmosphere have been corrected for telluric absorption. Where applied, the details of these corrections are discussed on a line-by-line basis.

3. ANALYSIS

3.1. Radial Velocities

The radial velocity for each star was determined in a two step process. An initial estimate of the radial velocity was ascertained by cross-correlation with a synthetic spectrum of a giant star with $T_{\text{eff}} = 4500 \text{ K}$, $\log g = 1.5$, and $[\text{M}/\text{H}] = -1.0$ across the wavelength range 845-870 nm. The observed spectrum was shifted to the pseudo-rest frame using this initial velocity estimate. Velocities found from cross-correlation are typically within 1 km s^{-1} of our final published value.

With our spectra at near-rest, we measured the equivalent widths of ~ 160 transitions by automatically fitting a Gaussian profile to the absorption lines (see Section 3.2). Fitted Gaussian profiles provide us with a measured equivalent width, the full-width half-maximum (FWHM) and the central wavelength of the profile. Thus, the residual radial velocity can be found directly from the ratio of the central and rest wavelengths. The final radial velocity for the star is provided by the initial velocity and the mean of ~ 160 residual line velocity measurements. Figure 1 shows the line velocities for HD 41667 after being placed at pseudo-rest using our cross-correlation velocity of 314.4 km s^{-1} . As expected, the mean residual offset is small (-0.75 km s^{-1}), and the standard deviation is 0.79 km s^{-1} from 164 measurements. This provides us with a final measured radial velocity of $313.6 \pm 0.1 \text{ kms}^{-1}$. This process was performed for all observations. The radial velocities published in Table 1 are the final values from this two step method. Heliocentric velocities agree quite well with those compiled by Williams et al. (2011) from the RAVE survey: the mean offset is $\langle \Delta V_{\text{hel}} \rangle = 2.5 \pm 2.7 \text{ km s}^{-1}$, demonstrating the accuracy of the velocities published in the RAVE catalog.

3.2. Line Measurements

For the measurement of atomic absorption lines, we employed the line list of Yong et al. (2005) with additional transitions of Cr, Sc, Zn, and Sr from Roederer et al. (2010). The list has been augmented with molecular CH data from Plez et al. (2008). For lines with hyperfine structure, blended transitions or molecular features, we determined the abundance using a spectral synthesis approach. For all other transitions, equivalent widths were measured to determine the line abundance.

The equivalent widths for all absorption lines were measured automatically using software written during this study. Given the rest wavelength and an initial guess of the FWHM, a Gaussian profile is iteratively fitted to

TABLE 1
OBSERVATIONS

Designation	α (J2000)	δ (J2000)	Observed Date	Airmass	Seeing (")	t_{exp} (secs)	S/N ^a (px ⁻¹)	V_{hel} (km s ⁻¹)	V_{err} (km s ⁻¹)
Standard Stars									
HD 41667	06:05:03.7	-32:59:36.8	2011-03-13	1.005	1.0	90	340	297.1	0.1
HD 44007	06:18:48.6	-14:50:44.2	2011-03-13	1.033	1.0	120	280	161.8	0.1
HD 76932	08:58:44.2	-16:07:54.2	2011-03-14	1.158	1.0	25	330	117.8	0.1
HD 136316	15:22:17.2	-53:14:13.9	2011-03-14	1.118	0.9	120	400	-38.8	0.1
HD 141531	15:49:16.9	+09:36:42.5	2011-03-14	1.309	0.9	120	350	2.8	0.1
HD 142948	16:00:01.6	-53:51:04.1	2011-03-14	1.107	1.0	90	320	29.9	0.1
Program Stars									
C222531-145437	22:25:31.7	-14:54:39.6	2011-07-30	1.033	0.8	650	135	-156.4	0.1
C230626-085103	23:06:26.6	-08:51:04.8	2011-07-30	1.096	1.0	650	100	-221.1	0.1
J221821-183424	22:18:21.2	-18:34:28.3	2011-07-30	1.026	0.9	650	115	-159.5	0.1
J223504-152834	22:35:04.5	-15:28:34.9	2011-07-30	1.047	1.0	650	130	-169.7	0.1
J223811-104126	22:38:11.6	-10:41:29.4	2011-07-30	1.218	1.2	650	115	-235.7	0.1

^a S/N measured at 600 nm for each target.

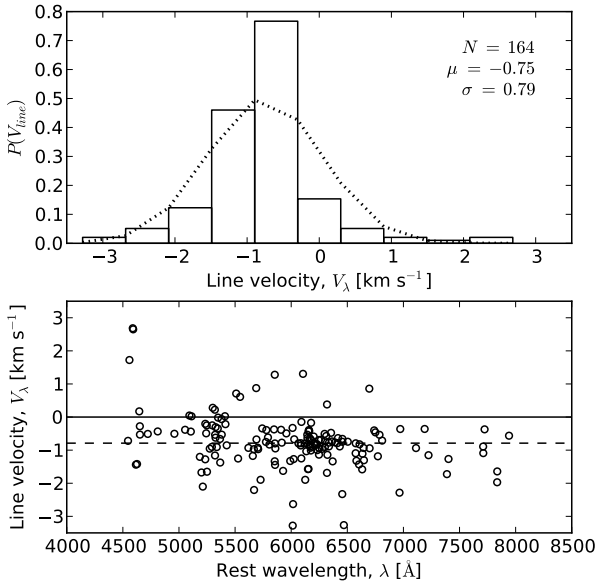


FIG. 1.— Residual velocities for each absorption line with a well-fitted Gaussian profile after correcting for doppler shift using the initial cross-correlation measurement. The mean residual velocity -0.75 km s^{-1} is within the $1-\sigma$ cross-correlation uncertainty of $\pm 0.9 \text{ km s}^{-1}$.

the absorption line. Simultaneously, the local continuum within 10 \AA either side of the rest wavelength is found by fitting a second-order polynomial. Measuring the local continuum ensures any errors in our initial normalisation or order-stitching do not propagate through to our equivalent width measurements. When determining the local continuum, any group of *neighbouring pixels* that all deviate significantly ($> 2\sigma$) from the local continua either belong to a persistent cosmic ray hit, or they are trough points of a nearby absorption profile. We attempt to fit a Gaussian profile to each group of deviating pixels, using the current best estimate for the local continuum. If a Gaussian profile is successfully fitted to the deviating group and its surrounding pixels, we assume the outlier

points – and all pixels included by that Gaussian profile – belong to an absorption line and are excluded from the iterative continuum determination.

When fitting Gaussian profiles, the χ^2 difference between the observed spectra and the fitted function is minimised. In order to account for crowded absorption regions where the χ^2 value might be influenced by a blended or strong nearby profile, our χ^2 function is weighted by the distance to the rest wavelength with the function,

$$W_{\lambda_i} = 1 + \exp\left(\frac{-(\lambda_i - \lambda_r)^2}{4\sigma^2}\right) \quad (1)$$

where the rest wavelength (λ_r) and profile sigma⁵ (σ) are free parameters in the iterative fitting process. As a consequence of Eq. 1, pixels near the rest wavelength are weighted slightly higher than those on the wings, forcing the fitting scheme to disregard blended or crowded surroundings. Although this approach relies on a reasonably accurate initial radial velocity correction of $< |4| \text{ km s}^{-1}$ – which is easily achieved – it greatly improves the accuracy and robustness of the equivalent width measurements.

The results of our iterative Gaussian fitting approach are *completely insensitive* to the initial FWHM guess. Increasing the initial FWHM estimate from 0.1 \AA to 1 or 2 \AA – which are unphysically large values for high-resolution spectra – does not alter either the measured FWHM or the equivalent width for any of our absorption lines. Only a small increase in computational cost is observed. Although we are extremely confident in our equivalent width measurements, *every* absorption profile was repeatedly examined by eye for quality, and spurious measurements were excluded.

We have verified the approach by comparing our measurements of 156 lines in HD 140283 with the study of Norris et al. (1996). We only included measurements in the Norris et al. (1996) study that were not marked with questionable line quality parameters. Excellent agreement is found between the two studies, which is illus-

⁵ Recall FWHM = $2\sigma\sqrt{2\log 2}$

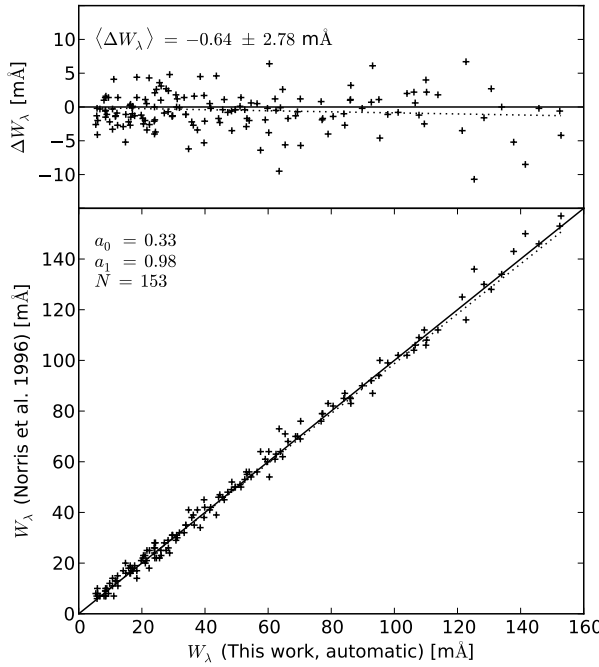


FIG. 2.— A comparison showing equivalent widths measured for HD 140283 using our automatic routine (see §3.2), and those found by careful hand measurements in Norris et al. (1996). No systematic trend is present, and the mean difference between these studies is $\langle \Delta W_\lambda \rangle = -0.64 \pm 2.78 \text{ m}\AA$.

trated in Figure 2. The mean difference is a negligible $-0.64 \pm 2.78 \text{ m}\AA$, and no systematic trend is present. We note that the scatter may be directly attributed to the observed S/N ratio, as other studies (Frebel et al. 2013) using the same equivalent width measurement software described here find better agreement with

hand measurements for spectra with higher S/N ratios: $0.20 \pm 0.16 \text{ m}\AA$ with Aoki et al. (2007) and $0.25 \pm 0.28 \text{ m}\AA$ with Cayrel et al. (2004) for a spectrum of HD 122563 with $S/N > 300 \text{ pixel}^{-1}$.

We list the atomic data and measured equivalent widths for transitions used during this analysis in Table 2. Saturated lines were excluded by removing measurements with reduced equivalent widths (REW), $\log_{10}(EW/\lambda) > -4.5 \text{ dex}$. A minimum detectable equivalent width was calculated as a function of wavelength based on the S/N ratio following Norris et al. (2001), and only lines that exceeded a 3σ detection significance were included.

3.3. Model Atmospheres

We have employed the ATLAS9 plane-parallel stellar atmospheres of Castelli & Kurucz (2003). These one-dimensional models ignore any centre-to-limb spatial variations, assume hydrostatic equilibrium and no convective overshoot from the photosphere. The stellar parameter spacing between models is 250 K, 0.5 dex in surface gravity, 0.5 dex in [M/H] and 0.1 dex in [α /Fe]. We interpolated the temperature, gas and radiative pressure, electron density and opacities between atmosphere models using the Quickhull algorithm (Barber et al. 1996). Quickhull is reliant on Delaunay tessellation, which suffers from extremely skewed cells when the grid points vary in size by orders of magnitude – as T_{eff} values do compared to $\log g$ or [M, α /H]. If unaccounted for, interpolating using such asymmetric cells can result in significant errors in atmospheric properties across all photospheric depths. We scaled each stellar parameter between zero and unity prior to interpolation in order to minimise these interpolation errors.

TABLE 2
List of Line Transitions and Equivalent Width Measurements

Wavelength (Å)	Transition	χ (eV)	$\log gf$	Equivalent Widths				
				C222531-145437 (mÅ)	C2306265-085103 (mÅ)	J221821-183424 (mÅ)	J223504-152834 (mÅ)	J223811-104126 (mÅ)
6300.300	8.0	0.00	-9.717	45.4	66.9	38.5	32.8	17.9
6363.780	8.0	0.02	-10.185	19.5	28.3	13.0	18.8	...
5688.190	11.0	2.11	-0.420	49.0	131.5	38.4
6154.230	11.0	2.10	-1.530	24.1	38.9	...	48.5	...
6160.750	11.0	2.10	-1.230	37.7	58.5	...	65.7	...
6318.720	12.0	5.11	-1.970	...	47.9	14.7	62.8	8.9
6319.240	12.0	5.11	-2.220	30.8	...	5.5
6965.410	12.0	5.75	-1.510	59.2	...
7387.690	12.0	5.75	-0.870	51.7	56.3	24.7	76.0	24.0
6696.020	13.0	3.14	-1.340	72.8	63.6	13.0
6698.670	13.0	3.14	-1.640	39.7	33.4	...	39.5	...
7835.310	13.0	4.02	-0.470	47.8	38.4	...	55.9	5.4
7836.130	13.0	4.02	-0.310	62.8	44.7	...	69.1	13.2
5690.430	14.0	4.93	-1.751	56.2	43.8	25.7	53.4	16.8
5793.070	14.0	4.93	-1.843	46.1	39.8	19.3	48.4	...
6125.020	14.0	5.61	-1.506	40.9	23.4	10.9	34.7	...
6145.010	14.0	5.62	-1.362	33.9	21.7	16.1	32.7	10.0
6155.130	14.0	5.62	-0.786	67.4	53.1	35.3	72.0	25.0
6166.440	20.0	2.52	-1.142	94.2	105.5	42.3	99.5	35.9
6169.040	20.0	2.52	-0.797	112.1	120.9	66.3	120.5	55.5
6169.560	20.0	2.53	-0.478	127.9	141.2	83.7	136.4	71.3
6455.600	20.0	2.52	-1.290	80.8	91.4	31.4	89.2	26.0
5526.820	21.1	1.77	0.130	98.8	113.3	100.8	98.4	51.1

TABLE 2
List of Line Transitions and Equivalent Width Measurements

Wavelength (Å)	Transition	χ (eV)	log gf	Equivalent Widths				
				C222531-145437 (mÅ)	C2306265-085103 (mÅ)	J221821-183424 (mÅ)	J223504-152834 (mÅ)	J223811-104126 (mÅ)
5657.880	21.1	1.51	-0.500	96.5	107.5	92.7	95.4	41.2
5667.150	21.1	1.50	-1.240	59.4	75.0	45.0	58.5	14.5
5669.040	21.1	1.50	-1.120	...	92.5	57.3	75.2	18.2
6245.610	21.1	1.51	-0.980	67.1	83.6	53.3	67.4	14.8
6604.600	21.1	1.36	-1.480	65.6	82.1	49.4	65.9	17.8
6064.630	22.0	1.05	-1.888	59.7	80.9	...	58.6	...
6091.170	22.0	2.27	-0.367	45.2	59.1	...	56.3	...
6312.240	22.0	1.46	-1.496	46.2	63.4	...	48.8	...
6336.100	22.0	1.44	-1.687	35.9	54.1	...	42.3	...
5154.080	22.1	1.57	-1.920	112.2	...	114.0	...	53.9
5185.910	22.1	1.89	-1.350	...	101.4	105.5	...	55.3
5336.790	22.1	1.58	-1.690	116.3	124.6	119.5	104.0	61.4
5381.030	22.1	1.59	-2.080	...	131.4	101.9	109.9	48.0
5727.060	23.0	1.08	-0.010	122.4	...	26.0	116.8	9.1
6090.220	23.0	1.08	-0.060	93.6	115.6	23.6	92.8	...
6216.360	23.0	0.28	-1.290	108.8	...	16.9	109.3	...
6251.820	23.0	0.29	-1.340	94.7	124.4	...	92.4	...
6274.640	23.0	0.27	-1.670	65.5	93.8	...	61.5	...
6504.160	23.0	1.18	-1.230	22.9	33.7	...	31.9	...
4545.950	24.0	0.94	-1.370	80.2
4580.056	24.0	0.94	-1.650	44.2
4616.137	24.0	0.98	-1.190	128.7	139.3	89.4	126.2	59.9
4626.188	24.0	0.97	-1.320	122.2	136.4	82.2	...	56.9
4646.150	24.0	1.03	-0.740	110.6	146.1	75.3
4651.280	24.0	0.98	-1.460	127.8	140.6	75.4	116.3	48.4
4652.158	24.0	1.00	-1.030	138.5	...	96.9	138.0	66.7
5206.040	24.0	0.94	0.020	132.8
5247.564	24.0	0.96	-1.640	141.4	...	76.1	...	46.7
5296.690	24.0	0.98	-1.360	149.9	...	85.0	141.0	59.0
5300.740	24.0	0.98	-2.000	120.5	112.2	...
5345.800	24.0	1.00	-0.950	115.4	...	81.1
5348.310	24.0	1.00	-1.210	150.8	...	94.8	142.4	63.0
5409.770	24.0	1.03	-0.670	132.4	...	92.1
4558.594	24.1	4.07	-0.656	101.8	46.5
4588.142	24.1	4.07	-0.826	46.0	53.0	60.5	55.0	36.0
4591.992	24.1	4.07	-1.419	29.1	28.5	19.6
6013.530	25.0	3.07	-0.251	89.2	114.6	22.2	109.4	14.8
6016.670	25.0	3.08	-0.100	94.0	116.0	28.1	113.0	17.1
6021.800	25.0	3.08	0.034	97.5	116.0	39.1	110.7	19.9
5044.210	26.0	2.85	-2.034	33.7
5054.640	26.0	3.64	-1.938	38.0
5242.490	26.0	3.63	-0.980	94.3	101.8	72.9	...	49.2
5321.110	26.0	4.43	-1.106	35.0	35.3	11.1
5322.040	26.0	2.28	-2.840	93.1	103.0	59.5	...	30.9
5326.140	26.0	3.57	-2.130	40.4	51.7	13.7	48.4	...
5365.400	26.0	3.57	-1.040	...	100.3	...	93.8	...
5367.480	26.0	4.41	0.430	108.4	118.0	92.4	119.1	73.7
5379.570	26.0	3.69	-1.530	71.4	81.4	34.9	75.6	19.6
5491.840	26.0	4.18	-2.250	17.3	...
5618.630	26.0	4.21	-1.292	43.5	54.3	20.2	57.4	11.3
5701.550	26.0	2.56	-2.216	118.5	134.8	91.8	119.5	49.5
5705.470	26.0	4.30	-1.420	29.2	41.5	10.9	44.5	7.7
5741.850	26.0	4.25	-1.689	36.2	37.0	13.0	48.2	...
5775.080	26.0	4.22	-1.310	55.0	62.1	25.3	67.4	14.7
5778.450	26.0	2.59	-3.480	42.8	55.8	13.4	50.1	...
5811.920	26.0	4.14	-2.430	10.9	...
5837.700	26.0	4.29	-2.340	12.9	...
5853.160	26.0	1.49	-5.280	30.4	43.4	6.3	34.7	...
5855.090	26.0	4.60	-1.547	13.3	20.3	...	22.8	...
5856.100	26.0	4.29	-1.640	27.9	40.2	...	42.7	...
5858.790	26.0	4.22	-2.260	...	11.4	...	16.9	...
5909.970	26.0	3.21	-2.640	56.0	72.6	18.5	63.3	...
5916.250	26.0	2.45	-2.994	92.9	105.1	51.2	95.4	17.7
5927.800	26.0	4.65	-1.090	32.4	36.7	12.2	50.9	...
5956.690	26.0	0.86	-4.608	121.7	143.8	70.3	107.8	25.5
6012.210	26.0	2.22	-4.070	44.4	58.8	11.5	53.0	...
6019.360	26.0	3.57	-3.360	7.0	11.3	...
6027.050	26.0	4.07	-1.106	66.2	77.0	36.2	77.2	23.5
6054.080	26.0	4.37	-2.310	5.6	8.1	...	12.9	...
6105.130	26.0	4.55	-2.050	...	10.9	...	14.8	...
6120.240	26.0	0.91	-5.970	35.2	52.7	8.5	32.4	...
6151.620	26.0	2.17	-3.299	88.9	102.9	46.9	87.0	18.2
6157.730	26.0	4.08	-1.320	...	81.2	33.2	78.1	18.8

TABLE 2
List of Line Transitions and Equivalent Width Measurements

Wavelength (Å)	Transition	χ (eV)	$\log gf$	Equivalent Widths				
				C222531-145437 (mÅ)	C2306265-085103 (mÅ)	J221821-183424 (mÅ)	J223504-152834 (mÅ)	J223811-104126 (mÅ)
6159.380	26.0	4.61	-1.970	...	9.6	...	13.6	...
6165.360	26.0	4.14	-1.490	40.6	51.6	14.2	54.0	10.8
6173.340	26.0	2.22	-2.880	109.6	125.6	70.7	105.6	34.9
6180.200	26.0	2.73	-2.637	86.2	100.6	44.3	91.5	20.8
6200.310	26.0	2.61	-2.437	105.2	122.2	70.8	105.4	36.6
6219.280	26.0	2.20	-2.433	134.3	153.3	103.3	127.4	56.7
6229.230	26.0	2.84	-2.846	60.1	73.1	21.0	65.8	13.6
6232.640	26.0	3.65	-1.283	92.6	104.3	58.3	103.0	35.6
6246.320	26.0	3.60	-0.894	114.0	129.2	90.5	124.1	61.7
6265.130	26.0	2.17	-2.550	132.9	155.0	94.8	129.7	55.5
6270.220	26.0	2.86	-2.500	76.7	93.6	41.2	79.1	17.4
6271.280	26.0	3.33	-2.728	31.6	44.9	13.4	43.6	...
6297.790	26.0	2.22	-2.740	119.3	...	81.3	111.3	42.3
6301.500	26.0	3.65	-0.766	115.0	130.6	91.1	117.9	...
6322.690	26.0	2.59	-2.426	111.0	124.4	74.2	103.5	41.6
6336.820	26.0	3.68	-0.916	106.6	116.8	81.2	113.6	52.8
6353.840	26.0	0.91	-6.477	11.8	23.7	...	14.1	...
6355.030	26.0	2.84	-2.403	...	122.2	58.9	...	27.8
6411.650	26.0	3.65	-0.734	122.5	135.1	97.8	131.8	68.2
6469.190	26.0	4.84	-0.770	18.7
6574.230	26.0	0.99	-5.004	84.1	118.5	35.4	87.0	...
6575.020	26.0	2.59	-2.727	100.7	118.2	55.5	103.4	23.4
6581.210	26.0	1.50	-4.705	72.4	87.5	21.7	69.6	...
6609.110	26.0	2.56	-2.692	102.0	118.8	60.9	103.1	29.1
6648.080	26.0	1.01	-5.918	37.1	54.9	...	37.9	...
6739.520	26.0	1.56	-4.820	43.1	60.8	...	44.5	...
6750.150	26.0	2.42	-2.621	110.9	128.9	78.6	109.5	40.2
6786.860	26.0	4.19	-1.850	22.5	29.1	...	32.3	...
6810.260	26.0	4.60	-1.000	36.2	46.9	14.5	54.9	8.5
6971.930	26.0	3.02	-3.390	21.0	30.3	...	28.7	...
7112.170	26.0	2.99	-3.044	45.4	59.3	13.3	53.0	...
7189.150	26.0	3.07	-2.796	57.5	66.3
7223.660	26.0	3.01	-2.269	87.2	114.4	47.2	90.8	...
7401.690	26.0	4.18	-1.660	38.9	50.5	14.7	59.7	...
7710.360	26.0	4.22	-1.129	62.5	76.7	32.5	75.4	...
7723.200	26.0	2.28	-3.617	82.1	100.4	36.6	91.9	...
7941.090	26.0	3.27	-2.331	50.3	...	22.4	61.7	...
5234.620	26.1	3.22	-2.150	...	81.2	58.3
5325.550	26.1	3.22	-3.220	...	32.1	43.4	...	11.6
5414.070	26.1	3.22	-3.750	23.6	21.0	6.8
5425.260	26.1	3.20	-3.370	27.1	38.2	41.3	37.3	14.5
5991.380	26.1	3.15	-3.557	21.5	...	28.3	25.8	7.7
6084.110	26.1	3.20	-3.808	11.8	16.0	20.0	18.8	...
6149.260	26.1	3.89	-2.724	21.7	25.2	30.8	26.3	11.8
6247.560	26.1	3.89	-2.329	31.2	36.7	50.2	40.3	21.4
6369.460	26.1	2.89	-4.250	13.5	16.3	18.1	16.7	5.9
6416.920	26.1	3.89	-2.740	23.1	29.2	29.2	31.9	...
6432.680	26.1	2.89	-3.708	30.0	33.6	41.7	37.5	12.9
6456.380	26.1	3.90	-2.075	40.9	47.9	61.2	49.3	30.9
7224.490	26.1	3.89	-3.243	12.7	13.2	...
7711.720	26.1	3.90	-2.543	23.7	29.1	37.4	29.8	14.9
6189.000	27.0	1.71	-2.450	51.1	77.5	9.1	58.7	...
6455.030	27.0	3.63	-0.250	19.1	29.8	...	31.4	...
6632.450	27.0	2.28	-2.000	29.1	42.3	...	34.7	...
5846.990	28.0	1.68	-3.210	60.7	77.0	17.8	62.7	...
6086.280	28.0	4.26	-0.515	31.8	36.1	12.4	47.8	...
6175.370	28.0	4.09	-0.535	41.4	48.6	21.1	52.5	10.4
6177.240	28.0	1.83	-3.510	39.3	48.8	11.1	39.4	...
6204.600	28.0	4.09	-1.140	14.9	18.5	...	25.3	...
6635.120	28.0	4.42	-0.828	14.9	18.2	...	26.0	...
6772.320	28.0	3.66	-0.987	53.5	59.1	26.5	62.0	13.0
5105.540	29.0	1.39	-1.520	139.4	160.4	67.1	123.3	32.5
4722.150	30.0	4.03	-0.390	74.1	67.9	73.6	76.5	37.4
4810.528	30.0	4.08	-0.137	61.5	63.6	72.5	82.3	42.1
7800.290	37.0	0.00	0.130	60.9	...
5123.220	39.1	0.99	-0.830	16.5
5200.420	39.1	0.99	-0.570	100.9	...	65.8	78.6	26.5
5509.910	39.1	0.99	-1.010	103.0	94.4	47.0	95.4	15.7
5544.610	39.1	1.74	-1.080	29.9	18.8	9.5	16.2	...
6127.440	40.0	0.15	-1.060	56.3	44.9	...	29.7	...
6134.550	40.0	0.00	-1.280	49.6	38.7	...	23.6	...
6143.200	40.0	0.07	-1.100	54.4	44.6	...	30.7	...
5112.270	40.1	1.67	-0.590	21.8

TABLE 2
List of Line Transitions and Equivalent Width Measurements

Wavelength (Å)	Transition	χ (eV)	$\log gf$	Equivalent Widths				
				C222531-145437 (mÅ)	C2306265-085103 (mÅ)	J221821-183424 (mÅ)	J223504-152834 (mÅ)	J223811-104126 (mÅ)
5853.640	56.1	0.60	-1.010	143.5	121.4	110.8	99.8	49.6
6141.730	56.1	0.70	-0.080	213.6	177.6	166.4	151.1	93.1
5805.770	57.1	0.13	-1.560	47.7	28.8	13.0	25.1	...
6390.480	57.1	0.32	-1.410	43.0	22.0	11.6	18.6	...
5274.240	58.1	1.04	-0.320	29.1	...	12.7
5472.300	58.1	1.24	-0.180	19.4
4959.120	60.1	0.06	-0.800	79.9	74.0	35.0	64.2	...
5092.790	60.1	0.38	-0.610	47.3	...	21.9	20.9	...
5212.360	60.1	0.20	-0.960	61.4	61.9	19.6	51.6	...
5234.190	60.1	0.55	-0.510	71.9	57.9	17.9	47.3	...
5249.580	60.1	0.98	0.200	64.5	54.7	31.8	50.7	...
5255.510	60.1	0.20	-0.670	116.3	...	40.5
5293.160	60.1	0.82	0.100	74.2	71.6	29.0	62.5	...
5319.810	60.1	0.55	-0.140	86.6	...	34.4
6645.110	63.1	1.38	0.204	24.5	27.8	17.0	30.3	...

3.4. Stellar Parameters

The May 2011 version of the spectral synthesis code MOOG (Sneden 1973) has been used to derive individual line abundances and stellar parameters. This version employs Rayleigh scattering (Sobeck et al. 2011) instead of treating scattering as true absorption, which is particularly important for transitions blue-ward of 450 nm. This is noteworthy, but is less relevant for these analyses as most of our line measurements are red-ward of 450 nm.

3.4.1. Effective Temperature

The effective temperature for each star was found by demanding a zero-trend in excitation potential and line abundance for measured Fe I and Fe II line abundances. A linear fit was made to the line abundances for each ionisation state, and gradients less than $|10^{-3}|$ dex were considered to be converged. Photometric temperatures were calculated after our spectroscopic temperatures had been derived, and are discussed in Section 3.4.4.

3.4.2. Microturbulence and Surface Gravity

The microturbulence for each star was found by forcing a zero-trend in REW and abundance for Fe I and II lines. Similarly for the effective temperature, gradients in REW and abundance of less than $|10^{-3}|$ dex were considered to be converged. The surface gravity for all stars was found by forcing the mean Fe I and Fe II abundances to be equal. The process is iterative: a zero trend with the excitation potential, reduced equivalent width and abundance must be maintained.

3.4.3. Metallicity, [M/H]

The degeneracy between stellar parameters requires a refinement of the stellar parameters until the line abundances were consistent with the model atmosphere. After these parameters had converged, the model metallicity was exactly matched to that of our mean Fe I abundance. Line abundances that were unusually deviant ($>3\sigma$) from the mean were removed. The largest number of outlier measurements removed for any observation was an uncomfortably large nine for C222531-145437 – which were near-saturated lines with REW ~ -4.5 – leaving 60 Fe I and 10 Fe II lines for analysis. For other candidates usually only one outlier measurement was removed. The

minimum number of iron transitions employed for stellar parameter determination in any star was 44 lines (33 Fe I and 11 Fe II) for our hottest star, J223811-104126.

3.4.4. Photometric Effective Temperatures

As a consistency check for our spectroscopic temperatures, we have estimated effective temperatures using infrared photometry from the 2MASS (Skrutskie et al. 2006) catalog and empirical T_{eff} -colour relationships. The $J - K$ colour has been employed for these calculations because it has the least dependence on metallicity.

The Aquarius stream is relatively close and at high-latitude, so significant extinction is not expected. The reddening maps of Schlegel et al. (1998) estimate that the extinction for our stars varies between $E(B - V) = 0.03$ to 0.07 mags. However, these maps are not perfect. As an alternative to using the Schlegel et al. (1998) dust maps, the level of extinction towards a star can be found directly by the strength of the interstellar Na D or K I lines (Munari & Zwitter 1997). The interstellar lines must be sufficiently separated from the stellar absorption features in order for the extinction to be measurable. This was the case in only one of our stars, J223811-104126. The equivalent width of the Na D1 line in J223811-104126 is found to be 302.4 mÅ, corresponding to an $E(B - V) = 0.12_{-0.02}^{+0.01}$ according to the Munari & Zwitter (1997) relationship. This is a significantly higher value than the Schlegel et al. (1998) reddening map suggests: $E(B - V) = 0.07$. For completeness, both extinction values have been used to calculate photometric temperatures.

Although all of our candidates are giant stars, two different T_{eff} -color relationships have been employed: the Alonso et al. (1999) calibration for giants, and the Casagrande et al. (2010) calibration for dwarfs and sub-giants. All photometrically-derived temperatures are listed in Table 4. For the Casagrande et al. (2010) dwarf/sub-giant $J - K$ relationship – which has a slight metallicity dependency – we have adopted the spectroscopically-derived [Fe/H] values shown in Table 3.

The effective temperatures found from spectroscopy agree fairly well with the photometric estimates. For three of our stars, the temperatures we find are in be-

tween the two color-temperature relationships. There are two noteworthy deviations: J223504-152834 and J223811-104126. For J223504-152834 we find the star to have an effective temperature of 4650 K, 71 K hotter than the Casagrande et al. (2010) dwarf/sub-giant relationship, yet 420 K hotter than the Alonso et al. (1999) estimate. Our temperature of 4650 K is in good agreement with previous spectroscopic determinations (4795 K; Williams et al. (2011), 4597 K; Wylie-de Boer et al. (2012)). The fact that the Alonso et al. (1999) photometric temperature relationship for giants predicts a temperature that is 420 K cooler than the spectroscopically-derived values may be attributed to an underestimated amount of dust towards J223504-152834. A higher than expected level of extinction along the line-of-sight would produce cooler photometric temperatures than the true effective temperature. An extinction of $E(B - V) = 0.10$ (up from 0.04) would be required for the Alonso et al. (1999) relation to yield a temperature of ~ 4500 K, which is within the uncertainties of our effective temperature derived from spectroscopy. Such a discrepancy in extinction is large, but not uncommon (e.g. see Peek & Graves 2010; Nataf et al. 2012, and the case of J223811-104126). Although we suspect J223504-152834 to have a higher reddening than $E(B - V) = 0.04$, we have adopted the Schlegel et al. (1998) value for distance determinations (see Section 3.7) as no extinction measurement could be ascertained from interstellar absorption lines.

J223811-104126, the second temperature deviant, has two extinction values available: the Schlegel et al. (1998) value of $E(B - V) = 0.07$ and the 0.12 value determined from the interstellar Na D1 line. Given the inherent difficulties in producing dust maps, we believe the $E(B - V) = 0.12$ determination to be more accurate. Employing the Schlegel et al. (1998) extinction value with the Alonso et al. (1999) color-temperature relationship yields good agreement (5104 K) with our spectroscopic temperature of 5190 K. Adopting our more accurate reddening determination yields 5215 K. The Casagrande et al. (2010) scale is ~ 200 K hotter in both cases.

With the exception of J223504-152834, the Alonso et al. (1999) giant relationship agrees well (± 100 K) with our spectroscopically-derived values. The Casagrande et al. (2010) relationship is also in reasonable agreement (most within 100 K, largest discrepancy is 300 K) with our spectroscopic temperatures, although we note that this relation was derived primarily for dwarfs/sub-giants and our candidates are giant stars.

3.5. Abundances

We have scaled our abundances to solar values using the Sun's chemical composition described in Asplund et al. (2009). The analysis of each element is discussed separately below in order of atomic number, with comparable elements grouped accordingly.

3.5.1. Carbon

Carbon is produced by the triple- α process and ejected in supernova events. Carbon abundances on the stellar surface increase as a star evolves along the red giant branch through dredge-up processes. While no atomic

carbon transitions exist in an optical spectrum, carbon is inferred from strong band heads and molecular features.

We have measured carbon abundances for all stars from the G-band head near 4313 Å and the CH band head at 4323 Å. Careful attention was paid to the normalisation of these regions. Synthetic spectra were computed for different carbon abundances in order to find the best fit with the observed spectrum. The abundances were determined separately for each band head and in all cases they agree within 0.10 dex of each other, which is less than the typical quoted uncertainty of 0.20 dex. The spectra were convolved with a Gaussian kernel, where the width was determined from synthesising spectra of nearby atomic lines that have known abundances from equivalent width measurements. A $^{12}\text{C}/^{13}\text{C}$ ratio of 4 was assumed, which provides a good fit to the data. An example fit to these regions for a standard and program star is shown in Figure 4.

Carbon abundances derived for our program stars agree well with the literature. For HD 136316 we find $[\text{C}/\text{Fe}] = -0.50 \pm 0.20$ dex, where Gratton et al. (2000) find $[\text{C}/\text{Fe}] = -0.66$ dex, and our $[\text{C}/\text{Fe}] = -0.48$ dex measurement for HD 141531 agrees within 0.06 dex. Most program stars have near-solar carbon abundances, ranging from $[\text{C}/\text{Fe}] = -0.30$ for J221821-183424, and +0.05 for J223811-104126.

3.5.2. Oxygen

Oxygen is a particularly difficult element to measure. There are only a handful of lines available in an optical spectrum: the forbidden $[\text{O I}]$ lines at 630 nm and 636 nm, and the O I triplet lines at 777 nm. The forbidden lines are very weak and become immeasurable in hot and/or metal-poor stars ($[\text{Fe}/\text{H}] \lesssim -1.5$ dex). When they are present, depending on the radial velocity of the star, the $[\text{O I}]$ lines can be significantly affected by telluric absorption. Moreover, the 630 nm line is blended with a Ni I absorption line (Allende Prieto et al. 2001). Hence the region requires careful consideration. Although the O I triplet lines at 777 nm are stronger than the forbidden lines, they are extremely susceptible to non-LTE effects and surface granulation (Asplund & García Pérez 2001), and sensitive to changes in microturbulence. Forbidden $[\text{O I}]$ abundances in our standard stars agree well with the literature, where an offset of -0.07 dex in $[\text{O}/\text{Fe}]$ is seen for HD 136316 when compared with Gratton et al. (2000).

The $[\text{O I}]$ lines were measurable in four of our Aquarius candidates. Careful consideration was taken when correcting for telluric absorption. The 630 nm line in one of our candidates, C2306265-085103, was sufficiently affected by telluric absorption such that we deemed the line unrecoverable. Thus, only the 636 nm transition was used to derive an oxygen abundance for C2306265-085103. In our hottest star, J223811-104126, the forbidden oxygen lines were not detected above a 3σ significance. After synthesising the region, we deduce a very conservative upper limit of $[\text{O}/\text{Fe}] < 0.50$ dex from the $[\text{O I}]$ lines. This is consistent with the rest of our candidates, with $[\text{O}/\text{Fe}]$ abundances varying between 0.43 to 0.49 dex.

In order to derive an oxygen measurement for J223811-104126, we were forced to use the triplet lines at

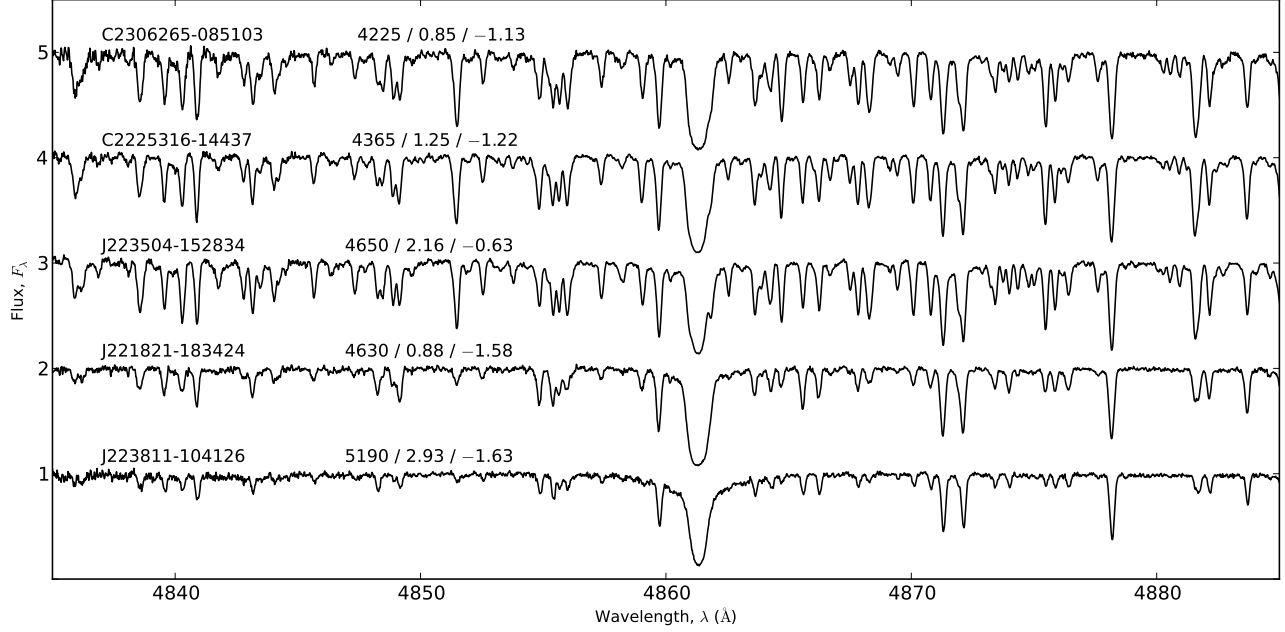


FIG. 3.— Normalised rest-frame spectra surrounding the H- β absorption line for all Aquarius stream candidates.

TABLE 3
STELLAR PARAMETERS

Designation	T_{eff} (K)	$\log g$ (dex)	v_t (km s $^{-1}$)	[Fe/H] (dex)	T_{eff} (K)	$\log g$ (dex)	v_t (km s $^{-1}$)	[Fe/H] (dex)	Source
Standard Stars									
HD 41667	4660	1.71	1.84	-1.20	4605	1.88	1.44	-1.16	Gratton et al. (2000)
HD 44007	4835	1.78	1.95	-1.77	4850	2.00	2.20	-1.71	Fulbright (2000)
HD 76932	5800	3.88	1.65	-1.05	5849	4.11	...	-0.88	Nissen et al. (2000)
HD 136316	4355	0.58	2.06	-1.93	4414	0.94	1.70	-1.90	Gratton & Sneden (1991)
HD 141531	4345	0.63	2.07	-1.69	4280	0.70	1.60	-1.68	Shetrone (1996)
HD 142948	5025	2.25	2.05	-0.74	4713	2.17	1.38	-0.77	Gratton et al. (2000)
Program Stars									
C222531-145437	4365	1.25	1.94	-1.22	4235 ± 118	1.45 ± 0.21	1.96 ± 0.11	-1.20 ± 0.14	Wylie-de Boer et al. (2012)
C230626-085103	4225	0.85	1.92	-1.13
J221821-183424	4630	0.88	2.16	-1.58	4395 ± 205	1.45 ± 0.35	1.96 ± 0.18	-1.15 ± 0.21	Wylie-de Boer et al. (2012)
J223504-152834	4650	2.16	1.55	-0.63	4597 ± 158	2.40 ± 0.14	1.47 ± 0.07	-0.98 ± 0.17	Wylie-de Boer et al. (2012)
J223811-104126	5190	2.93	1.62	-1.63	5646 ± 147	4.60 ± 0.15	1.09 ± 0.11	-1.20 ± 0.20	Wylie-de Boer et al. (2012)

TABLE 4
REDDENING & PHOTOMETRIC TEMPERATURES

Designation	$E(B-V)$ (mag)	$(J-K)_0$	T_{phot}	
			Alonso (K)	Casagrande (K)
C222531-145437	0.03	0.75	4247	4391
C230626-085103	0.05	0.82	4091	4200
J221821-183424	0.03	0.64	4546	4747
J223504-152834	0.04	0.69	4110	4579
J223811-104126	0.07	0.48	5104	5367
	0.12 ^a	0.45	5215	5484

^aExtinction derived from interstellar Na D1 line (see 3.4.4)

777 nm. Each line was synthesised and a mean abundance was calculated for each candidate. Abundances determined from the oxygen triplet lines were system-

atically +0.27 dex higher than that found from the [O I] forbidden lines. García Pérez et al. (2006) found [O/Fe] values based on the O I permitted triplet lines are on average $+0.19 \pm 0.07$ dex higher than those found from the forbidden lines, which did not include non-LTE corrections of +0.08 dex. Thus, we attribute our +0.27 dex offset between measurements of the [O I] and O I triplet lines to non-LTE and 3D effects as it is precisely the same as the total difference found by García Pérez et al. (2006). García Pérez et al. (2006) concluded that the forbidden lines, when not too weak, probably give the most reliable estimate of oxygen abundance.

From the permitted O I triplet, we derive an oxygen abundance of $[\text{O}/\text{Fe}] = 0.42 \pm 0.01$ dex (random scatter) for J223811-104126. This measurement will be systematically higher than the ‘true’ abundance if it were discernible from the [O I] lines, on the order of $\sim +0.27$ dex.

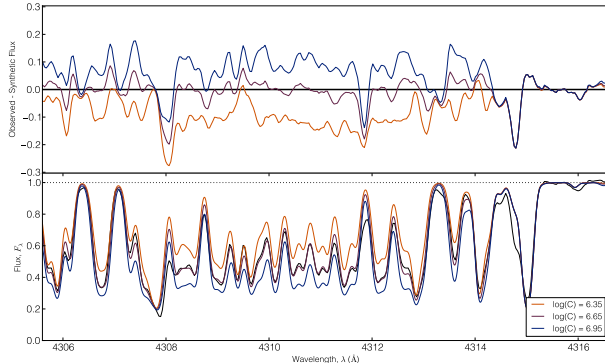


FIG. 4.— The Carbon CH band near 4313 Å in our standard star HD 44007. The best-fit synthetic spectra is shown, with uncertainties in $\log_e C$ of ± 0.20 dex – the smallest uncertainty assumed from synthetic spectral fits.

When we apply this crude offset derived from the rest of our sample, we arrive at a corrected abundance of $[\text{O}/\text{Fe}] = 0.15 \pm 0.08$ dex for J223811-104126. This is the most oxygen-deficient star in our sample by a factor of two.

3.5.3. Sodium

Our line list includes three clean, unblended sodium lines at 5688 Å, 6154 Å and 6161 Å. Not all three of these lines were detectable in each star. In the hottest and most metal-poor stars, J223811-104126 and J221821-183424 respectively, only the 5688 Å line was measurable. Consequently, an uncertainty of ± 0.10 dex was adopted for these stars. For stars where multiple sodium lines were available, the line-to-line scatter is reasonable: usually around 0.04 dex with a maximum of 0.09 dex in HD 41667.

Our $[\text{Na}/\text{Fe}]$ abundances appear systematically higher than values found in the literature, on the order of 0.10 dex. For HD 142948 we yield $[\text{Na}/\text{Fe}] = 0.22$ dex, which is +0.10 dex higher than that found for Gratton et al. (2000), and similarly we find HD 76932 to be +0.10 dex higher than reported by Fulbright (2000). Gratton et al. (2000) also found HD 136316 to have $[\text{Na}/\text{Fe}] = -0.29$ dex, where we find $[\text{Na}/\text{Fe}] = -0.14$ dex where there is excellent agreement in the stellar parameters. Different solar compositions employed between this study and earlier work can account for ~ 0.08 dex of this effect, leaving the residual difference well within the observational uncertainties. However, it is important to note that the $[\text{Na}/\text{Fe}]$ abundance ratios presented may be higher compared to previous studies.

3.5.4. α -elements (Mg , Si , Ca and Ti)

The α -elements (Mg , Si , Ca and Ti) are forged through α -particle capture in assorted burning stages of stellar evolution, including the burning of carbon, neon and silicon. Although Si and Ti ($Z = 14, 22$) are not formally α -elements, their abundance generally varies with those of the other α -elements and therefore has been included here.

Depending on the radial velocity of the star, some magnesium lines were affected by telluric absorption, particularly the 6318 and 6965 Å transitions. Atmospheric absorption was most notable for C222531-145437, where

three of the four Mg transitions in our line list suffered some degree of telluric absorption, requiring an attentive correction. Every amended absorption profile was carefully examined, and lines with suspicious profiles were excluded from the final magnesium abundance. All $[\alpha/\text{Fe}]$ abundance ratios in the standard stars are in excellent agreement with the literature. Typically the difference is 0.01 dex, with the largest discrepancy of $\Delta[\text{Ti}/\text{Fe}] = +0.13$ dex for HD 76932 when compared with Fulbright (2000).

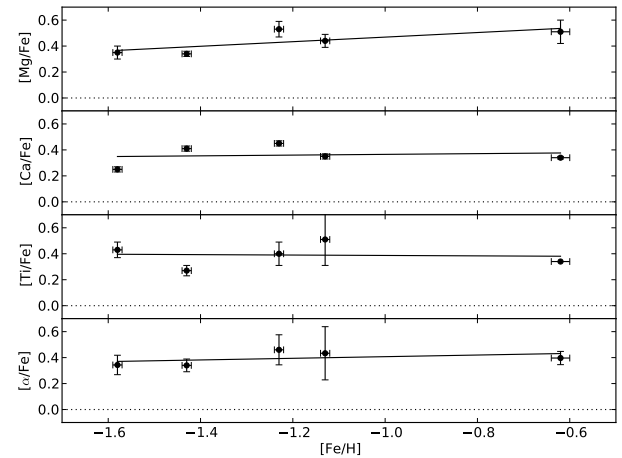


FIG. 5.— The α -element abundances with respect to iron content. The mean $[\alpha/\text{Fe}]$ abundance from these is shown in the bottom panel.

Of all the α -elements, calcium has the smallest measurement scatter in our stars. The mean was formed from four line measurements in each star, with the typical measurement uncertainty was 0.01 dex. As shown in Figure 5, all Aquarius candidates show super-solar $[\text{Ca}/\text{Fe}]$, ranging between +0.23 to +0.43 dex, consistent with $[\text{Mg}, \text{Ti}, \text{Si}/\text{Fe}]$ measurements.

However, C222531-145437 has an unusually high silicon abundance ($[\text{Si}/\text{Fe}] = 0.79$ dex), well outside the uncertainties of the rest of our sample. The silicon line abundances in this star are in relatively good agreement with one another. If we exclude the highest line measurement, then the mean abundance drops only slightly to $[\text{Si}/\text{Fe}] = 0.73 \pm 0.04$ dex. The lowest silicon line abundance for C222531-145437 is $[\text{Si}/\text{Fe}] = 0.61$ dex, which is still significantly higher than the mean abundance for any other star.

Titanium abundances for the stream stars are generally in agreement with one another, showing typical α -enhancement signatures. Our mean titanium abundances are derived from four to seven clean, unblended lines. In our hottest and most metal-poor stars, no suitable Ti I transitions were available. In other stream candidates, the mean difference between species is $\langle \text{Ti I} - \text{Ti II} \rangle = 0.24$ dex. Although this discrepancy is not negligible, there are limited lines available for comparison and our mean $\langle \text{Fe I} - \text{Fe II} \rangle$, $\langle \text{Cr I} - \text{Cr II} \rangle$ (see Section 3.5.6) differences are very small.

TABLE 5
Standard Star Abundances

Species	<i>N</i>	$\log \epsilon(X)$	σ_ϵ	[X/H]	[X/Fe]	σ	Species	<i>N</i>	$\log \epsilon(X)$	σ_ϵ	[X/H]	[X/Fe]	σ
HD 41667							HD 44007						
C (CH)	2	6.95	0.20	-1.48	-0.28	0.20	C (CH)	2	6.66	0.20	-1.77	-0.01	0.20
O I	2	7.95	0.06	-0.74	0.46	0.04	O I	1	7.41	0.00	-1.28	0.48	0.00
Na I	3	4.90	0.18	-1.34	-0.14	0.10	Na I	2	4.44	0.09	-1.80	-0.04	0.06
Mg I	4	6.72	0.10	-0.88	0.32	0.05	Mg I	2	6.30	0.06	-1.29	0.47	0.04
Al I	4	5.18	0.11	-1.27	-0.07	0.06	Al I	1	4.80	0.00	-1.65	0.11	0.00
Si I	5	6.55	0.06	-0.96	0.24	0.03	Si I	5	6.07	0.07	-1.44	0.32	0.03
K I	1	4.64	0.00	-0.39	0.81	0.00	K I	1	4.31	0.00	-0.72	1.04	0.00
Ca I	4	5.47	0.06	-0.87	0.33	0.03	Ca I	4	4.95	0.02	-1.39	0.37	0.01
Sc II	6	2.13	0.13	-1.02	0.18	0.05	Sc II	6	1.39	0.10	-1.76	0.00	0.04
Ti I	4	3.96	0.04	-0.99	0.21	0.02	Ti I	1	3.48	0.00	-1.47	0.29	0.00
Ti II	3	4.09	0.25	-0.86	0.35	0.14	Ti II	4	3.47	0.15	-1.48	0.28	0.07
V I	6	2.87	0.13	-1.06	0.14	0.05	V I	4	2.17	0.03	-1.77	-0.00	0.01
Cr I	10	4.22	0.08	-1.42	-0.22	0.03	Cr I	15	3.65	0.07	-1.99	-0.22	0.02
Cr II	2	4.54	0.05	-1.09	0.11	0.04	Cr II	3	4.00	0.01	-1.64	0.12	0.01
Mn I	3	3.96	0.01	-1.47	-0.27	0.01	Mn I	3	3.15	0.04	-2.28	-0.52	0.02
Fe I	61	6.30	0.12	-1.20	0.00	0.02	Fe I	51	5.74	0.13	-1.76	0.00	0.02
Fe II	13	6.35	0.05	-1.15	0.05	0.01	Fe II	15	5.74	0.10	-1.76	-0.00	0.03
Co I	5	3.75	0.10	-1.24	-0.04	0.04	Co I	1	3.22	0.00	-1.77	-0.01	0.00
Ni I	7	4.94	0.12	-1.28	-0.08	0.05	Ni I	4	4.47	0.05	-1.75	0.01	0.02
Cu I	1	2.72	0.00	-1.47	-0.27	0.00	Cu I	1	1.84	0.00	-2.35	-0.59	0.00
Zn I	2	3.36	0.08	-1.20	0.00	0.06	Zn I	2	2.83	0.05	-1.73	0.03	0.04
Sr I	1	1.31	0.00	-1.56	-0.36	0.00	Sr I	1	0.91	0.00	-1.96	-0.20	0.00
Y II	5	0.97	0.19	-1.24	-0.04	0.09	Y II	6	0.28	0.11	-1.93	-0.16	0.05
Zr I	2	1.42	0.05	-1.17	0.04	0.04	Zr I	0
Zr II	1	1.28	0.00	-1.30	-0.10	0.00	Zr II	1	0.59	0.00	-1.99	-0.23	0.00
Ba II	2	1.02	0.04	-1.16	0.05	0.02	Ba II	2	0.25	0.01	-1.93	-0.17	0.01
La II	2	0.14	0.04	-0.96	0.24	0.03	La II	2	-0.52	0.02	-1.62	0.14	0.01
Ce II	4	0.35	0.18	-1.23	-0.02	0.09	Ce II	3	-0.41	0.12	-1.99	-0.23	0.07
Nd II	9	0.54	0.10	-0.88	0.32	0.03	Nd II	9	-0.36	0.11	-1.78	-0.01	0.04
Eu II	1	-0.05	0.00	-0.57	0.63	0.00	Eu II	1	-0.36	0.00	-0.88	0.88	0.00
HD 76932							HD 136316						
C (CH)	2	7.52	0.20	-0.91	0.14	0.20	C (CH)	2	5.95	0.20	-2.48	-0.50	0.20
O I	0	O I	1	7.17	0.00	-1.52	0.41	0.00
Na I	3	5.37	0.04	-0.87	0.18	0.02	Na I	2	4.17	0.04	-2.08	-0.14	0.02
Mg I	3	6.95	0.20	-0.65	0.40	0.11	Mg I	2	6.08	0.24	-1.52	0.41	0.17
Al I	4	5.45	0.07	-1.00	0.05	0.03	Al I	0
Si I	5	6.79	0.06	-0.72	0.33	0.03	Si I	4	5.89	0.05	-1.62	0.31	0.03
K I	1	4.94	0.00	-0.09	0.96	0.00	K I	1	3.91	0.00	-1.12	0.81	0.00
Ca I	4	5.60	0.02	-0.74	0.31	0.01	Ca I	4	4.71	0.02	-1.63	0.30	0.01
Sc II	6	2.25	0.11	-0.90	0.16	0.04	Sc II	5	1.30	0.05	-1.85	0.08	0.02
Ti I	1	4.36	0.00	-0.59	0.46	0.00	Ti I	3	3.19	0.03	-1.76	0.17	0.02
Ti II	3	4.33	0.04	-0.62	0.44	0.02	Ti II	3	3.44	0.10	-1.51	0.42	0.06
V I	3	3.17	0.13	-0.76	0.29	0.08	V I	5	1.87	0.07	-2.06	-0.13	0.03
Cr I	15	4.46	0.05	-1.18	-0.13	0.01	Cr I	12	3.49	0.05	-2.15	-0.22	0.01
Cr II	3	4.76	0.02	-0.88	0.17	0.01	Cr II	2	3.90	0.02	-1.74	0.19	0.01
Mn I	3	4.08	0.03	-1.35	-0.29	0.02	Mn I	3	3.08	0.02	-2.35	-0.42	0.01
Fe I	51	6.45	0.10	-1.05	0.00	0.01	Fe I	62	5.57	0.11	-1.93	0.00	0.01
Fe II	13	6.50	0.07	-1.00	0.05	0.02	Fe II	14	5.61	0.12	-1.89	0.04	0.03
Co I	3	4.10	0.06	-0.89	0.16	0.03	Co I	6	3.11	0.07	-1.88	0.05	0.03
Ni I	5	5.29	0.02	-0.93	0.13	0.01	Ni I	5	4.22	0.11	-2.00	-0.07	0.05
Cu I	1	2.84	0.00	-1.35	-0.30	0.00	Cu I	1	1.73	0.00	-2.46	-0.53	0.00
Zn I	2	3.58	0.03	-0.98	0.07	0.02	Zn I	2	2.72	0.03	-1.83	0.10	0.02
Sr I	1	1.65	0.00	-1.22	-0.17	0.00	Sr I	1	0.53	0.00	-2.34	-0.41	0.00
Y II	5	1.14	0.05	-1.07	-0.02	0.02	Y II	7	0.12	0.11	-2.09	-0.16	0.04
Zr I	0	Zr I	1	0.79	0.00	-1.79	0.14	0.00
Zr II	0	Zr II	1	0.68	0.00	-1.90	0.03	0.00
Ba II	1	1.16	0.00	-1.02	0.03	0.00	Ba II	1	0.22	0.00	-1.96	-0.03	0.00
La II	1	0.61	0.00	-0.49	0.56	0.00	La II	2	-0.68	0.03	-1.78	0.16	0.02
Ce II	2	0.37	0.03	-1.21	-0.16	0.02	Ce II	5	-0.39	0.18	-1.97	-0.04	0.08
Nd II	3	0.56	0.06	-0.86	0.19	0.03	Nd II	10	-0.36	0.04	-1.78	0.15	0.01
Eu II	1	-0.01	0.00	-0.53	0.52	0.00	Eu II	1	-1.07	0.00	-1.59	0.34	0.00
HD 141531							HD 142948						
C (CH)	2	6.33	0.20	-2.10	-0.48	0.20	C (CH)	2	7.72	0.20	-0.71	0.03	0.20
O I	2	7.33	0.01	-1.35	0.34	0.01	O I	2	8.43	0.02	-0.26	0.47	0.02
Na I	2	4.28	0.05	-1.96	-0.27	0.04	Na I	3	5.73	0.13	-0.51	0.22	0.08
Mg I	2	6.30	0.15	-1.29	0.40	0.10	Mg I	3	7.24	0.12	-0.36	0.38	0.07
Al I	2	4.74	0.10	-1.71	-0.02	0.07	Al I	4	5.94	0.08	-0.51	0.23	0.04
Si I	5	6.03	0.10	-1.48	0.21	0.04	Si I	5	7.07	0.05	-0.44	0.30	0.02
K I	1	3.99	0.00	-1.04	0.65	0.00	K I	1	5.04	0.00	0.01	0.75	0.00

Continued..

TABLE 5
Standard Star Abundances

Species	<i>N</i>	$\log \epsilon(X)$	σ_ϵ	[X/H]	[X/Fe]	σ	Species	<i>N</i>	$\log \epsilon(X)$	σ_ϵ	[X/H]	[X/Fe]	σ
Ca I	4	4.90	0.03	-1.44	0.25	0.01	Ca I	4	5.78	0.01	-0.56	0.18	0.01
Sc II	4	1.56	0.04	-1.59	0.10	0.02	Sc II	6	2.57	0.11	-0.58	0.16	0.05
Ti I	4	3.33	0.07	-1.62	0.07	0.03	Ti I	4	4.44	0.09	-0.51	0.23	0.04
Ti II	4	3.71	0.08	-1.24	0.46	0.04	Ti II	3	4.40	0.21	-0.55	0.19	0.12
V I	5	2.12	0.07	-1.81	-0.11	0.03	V I	5	3.31	0.11	-0.62	0.12	0.05
Cr I	12	3.68	0.06	-1.96	-0.27	0.02	Cr I	13	4.67	0.15	-0.97	-0.23	0.04
Cr II	2	4.11	0.02	-1.53	0.16	0.01	Cr II	3	4.88	0.03	-0.76	-0.02	0.02
Mn I	3	3.29	0.04	-2.14	-0.45	0.02	Mn I	3	4.54	0.03	-0.89	-0.15	0.02
Fe I	54	5.81	0.06	-1.69	0.00	0.01	Fe I	61	6.76	0.10	-0.74	0.00	0.01
Fe II	13	5.86	0.03	-1.64	0.05	0.01	Fe II	13	6.75	0.06	-0.75	-0.02	0.02
Co I	5	3.23	0.09	-1.76	-0.07	0.04	Co I	5	4.42	0.08	-0.57	0.17	0.03
Ni I	7	4.42	0.12	-1.80	-0.11	0.04	Ni I	5	5.62	0.04	-0.60	0.13	0.02
Cu I	1	2.03	0.00	-2.16	-0.47	0.00	Cu I	1	3.53	0.00	-0.66	0.08	0.00
Zn I	2	2.80	0.04	-1.76	-0.07	0.03	Zn I	2	3.89	0.06	-0.67	0.07	0.04
Sr I	1	0.66	0.00	-2.21	-0.52	0.00	Sr I	1	1.67	0.00	-1.20	-0.46	0.00
Y II	6	0.27	0.13	-1.94	-0.24	0.05	Y II	6	1.33	0.32	-0.88	-0.14	0.13
Zr I	0	Zr I	0
Zr II	1	0.75	0.00	-1.83	-0.14	0.00	Zr II	0
Ba II	1	0.40	0.00	-1.78	-0.09	0.00	Ba II	2	1.18	0.01	-1.00	-0.26	0.01
La II	2	-0.55	0.08	-1.66	0.04	0.05	La II	2	0.43	0.12	-0.67	0.07	0.08
Ce II	4	-0.31	0.12	-1.89	-0.20	0.06	Ce II	3	0.54	0.20	-1.04	-0.30	0.11
Nd II	10	-0.20	0.08	-1.62	0.07	0.02	Nd II	6	0.79	0.10	-0.63	0.11	0.04
Eu II	1	-0.83	0.00	-1.35	0.34	0.00	Eu II	1	0.16	0.00	-0.36	0.38	0.00

TABLE 6
Program Star Abundances

Species	<i>N</i>	$\log \epsilon(X)$	σ_ϵ	[X/H]	[X/Fe]	σ	Species	<i>N</i>	$\log \epsilon(X)$	σ_ϵ	[X/H]	[X/Fe]	σ
J221821-183424													
C (CH)	2	6.55	0.20	-1.88	-0.30	0.25	C (CH)	2	7.15	0.20	-1.28	-0.05	0.20
O I	2	7.55	0.04	-1.13	0.45	0.02	O I	2	7.96	0.00	-0.73	0.49	0.00
Na I	1	4.75	0.00	-1.49	0.09	0.00	Na I	2	5.12	0.02	-1.12	0.10	0.01
Mg I	3	6.37	0.09	-1.23	0.35	0.05	Mg I	2	6.90	0.08	-0.70	0.53	0.06
Al I	1	5.08	0.00	-1.37	0.21	0.00	Al I	4	5.94	0.10	-0.51	0.71	0.05
Si I	5	6.32	0.08	-1.19	0.39	0.04	Si I	5	7.07	0.15	-0.44	0.79	0.07
K I	1	4.34	0.00	-0.69	0.89	0.00	K I	1	4.42	0.00	-0.61	0.62	0.00
Ca I	4	5.01	0.04	-1.33	0.25	0.02	Ca I	4	5.57	0.04	-0.77	0.45	0.02
Sc II	6	1.53	0.08	-1.62	-0.04	0.03	Sc II	5	2.11	0.12	-1.04	0.19	0.06
Ti I	0	Ti I	4	4.10	0.03	-0.85	0.37	0.01
Ti II	4	3.80	0.13	-1.15	0.43	0.06	Ti II	2	4.12	0.13	-0.83	0.40	0.09
V I	3	2.28	0.01	-1.65	-0.07	0.01	V I	6	3.02	0.16	-0.92	0.31	0.06
Cr I	11	3.80	0.06	-1.84	-0.26	0.02	Cr I	8	4.24	0.17	-1.40	-0.17	0.06
Cr II	2	4.07	0.03	-1.57	0.01	0.02	Cr II	1	4.38	0.00	-1.26	-0.03	0.00
Mn I	3	3.35	0.03	-2.08	-0.49	0.02	Mn I	3	4.20	0.04	-1.23	-0.01	0.03
Fe I	52	5.92	0.09	-1.58	0.00	0.01	Fe I	60	6.27	0.10	-1.23	0.00	0.01
Fe II	13	5.94	0.05	-1.56	0.02	0.01	Fe II	10	6.30	0.06	-1.20	0.03	0.02
Co I	4	3.32	0.16	-1.67	-0.09	0.08	Co I	5	3.92	0.12	-1.07	0.15	0.05
Ni I	5	4.61	0.14	-1.61	-0.03	0.06	Ni I	7	5.07	0.09	-1.15	0.08	0.04
Cu I	1	2.18	0.00	-2.01	-0.43	0.00	Cu I	1	3.33	0.00	-0.86	0.37	0.00
Zn I	1	3.07	0.00	-1.49	0.09	0.00	Zn I	2	3.56	0.24	-1.00	0.23	0.17
Sr I	1	0.82	0.00	-2.05	-0.47	0.00	Sr I	1	1.55	0.00	-1.32	-0.09	0.00
Sr II	0	Sr II	0
Y II	3	0.44	0.02	-1.77	-0.19	0.01	Y II	5	1.78	0.16	-0.43	0.79	0.07
Zr I	0	Zr I	3	2.07	0.05	-0.51	0.72	0.03
Zr II	1	0.97	0.00	-1.61	-0.03	0.00	Zr II	0
Ba II	2	0.60	0.05	-1.58	0.00	0.04	Ba II	3	1.58	0.02	-0.60	0.62	0.01
La II	2	-0.47	0.00	-1.57	0.01	0.00	La II	2	0.55	0.00	-0.55	0.68	0.00
Ce II	3	-0.39	0.06	-1.97	-0.39	0.03	Ce II	5	0.73	0.15	-0.85	0.37	0.07
Nd II	10	-0.22	0.07	-1.64	-0.06	0.02	Nd II	8	0.88	0.13	-0.54	0.69	0.05
Eu II	2	-0.10	0.65	-0.62	0.96	0.46	Eu II	1	-0.19	0.00	-0.71	0.52	0.00
J223504-152834													
J223811-104126													
C (CH)	2	7.71	0.30	-0.72	-0.10	0.30	C (CH)	2	7.05	0.25	-1.38	0.05	0.25
O I	2	8.50	0.10	-0.19	0.43	0.07	O I	1	8.27	0.00	-0.42	0.15 ⁶	0.08
Na I	3	5.87	0.12	-0.37	0.26	0.07	Na I	1	4.89	0.00	-1.35	0.08	0.00
Mg I	3	7.48	0.15	-0.12	0.51	0.09	Mg I	2	6.51	0.03	-1.09	0.34	0.02
Al I	3	6.12	0.09	-0.33	0.29	0.05	Al I	2	5.13	0.13	-1.32	0.11	0.10
Si I	5	7.24	0.10	-0.27	0.35	0.05	Si I	3	6.42	0.04	-1.09	0.34	0.02

Continued..

⁶ Abundance derived from the permitted O I triplet instead of the forbidden [O I] lines, see §3.5.2.

TABLE 6
 Program Star Abundances

Species	<i>N</i>	$\log \epsilon(X)$	σ_ϵ	[X/H]	[X/Fe]	σ	Species	<i>N</i>	$\log \epsilon(X)$	σ_ϵ	[X/H]	[X/Fe]	σ
K I	1	5.05	0.00	0.02	0.64	0.00	K I	1	4.50	0.00	-0.53	0.90	0.00
Ca I	4	6.06	0.03	-0.28	0.34	0.01	Ca I	4	5.32	0.03	-1.02	0.41	0.02
Sc II	6	2.74	0.14	-0.41	0.22	0.06	Sc II	6	1.72	0.14	-1.43	-0.00	0.06
Ti I	4	4.65	0.02	-0.30	0.32	0.01	Ti I	0
Ti II	1	4.67	0.00	-0.28	0.34	0.00	Ti II	4	3.79	0.09	-1.16	0.27	0.04
V I	4	3.59	0.10	-0.34	0.28	0.05	V I	1	2.45	0.00	-1.48	-0.05	0.00
Cr I	7	4.90	0.11	-0.74	-0.11	0.04	Cr I	12	4.10	0.06	-1.54	-0.11	0.02
Cr II	2	4.84	0.04	-0.79	-0.17	0.03	Cr II	3	4.34	0.07	-1.30	0.12	0.04
Mn I	3	5.06	0.10	-0.37	0.25	0.06	Mn I	3	3.58	0.04	-1.85	-0.43	0.02
Fe I	63	6.88	0.12	-0.62	0.00	0.02	Fe I	33	6.07	0.06	-1.43	-0.00	0.01
Fe II	12	6.87	0.07	-0.63	-0.01	0.02	Fe II	9	6.04	0.07	-1.46	-0.03	0.02
Co I	5	4.59	0.14	-0.40	0.22	0.06	Co I	0
Ni I	7	5.64	0.09	-0.58	0.05	0.03	Ni I	2	4.84	0.04	-1.38	0.05	0.03
Cu I	1	3.81	0.00	-0.38	0.24	0.00	Cu I	1	2.40	0.00	-1.79	-0.36	0.00
Zn I	2	4.21	0.03	-0.35	0.27	0.02	Zn I	2	3.15	0.05	-1.41	0.02	0.04
Sr I	1	1.83	0.00	-1.04	-0.42	0.00	Sr I	1	1.23	0.00	-1.64	-0.21	0.00
Sr II	0	Sr II	0
Y II	3	1.80	0.03	-0.41	0.21	0.02	Y II	6	0.76	0.06	-1.45	-0.02	0.03
Zr I	3	2.26	0.05	-0.32	0.31	0.03	Zr I	0
Zr II	0	Zr II	0
Ba II	2	1.65	0.02	-0.53	0.10	0.01	Ba II	2	0.70	0.03	-1.48	-0.05	0.02
La II	2	0.74	0.05	-0.36	0.26	0.04	La II	0
Ce II	3	0.87	0.13	-0.71	-0.09	0.08	Ce II	2	-0.07	0.02	-1.65	-0.22	0.02
Nd II	6	1.27	0.13	-0.15	0.47	0.06	Nd II	1	-0.25	0.00	-1.67	-0.24	0.00
Eu II	1	0.52	0.00	0.00	0.62	0.00	Eu II	1	-0.55	0.00	-1.07	0.36	0.00

C2306265-085103						
C (CH)	2	7.20	0.20	-1.23	-0.10	0.20
O I	2	8.02	0.04	-0.67	0.46	0.03
Na I	2	5.31	0.01	-0.93	0.21	0.00
Mg I	2	6.90	0.06	-0.70	0.44	0.05
Al I	4	5.65	0.08	-0.80	0.33	0.04
Si I	5	6.78	0.08	-0.73	0.40	0.04
K I	1	4.46	0.00	-0.57	0.56	0.00
Ca I	4	5.56	0.04	-0.78	0.35	0.02
Sc II	6	2.28	0.16	-0.87	0.26	0.06
Ti I	4	4.13	0.03	-0.82	0.32	0.01
Ti II	3	4.32	0.35	-0.63	0.51	0.20
V I	4	2.96	0.05	-0.98	0.16	0.03
Cr I	3	4.13	0.12	-1.51	-0.38	0.07
Cr II	1	4.50	0.00	-1.14	-0.01	0.00
Mn I	3	4.40	0.10	-1.03	0.10	0.06
Fe I	62	6.37	0.12	-1.13	0.00	0.01
Fe II	11	6.39	0.10	-1.11	0.02	0.03
Co I	5	4.14	0.14	-0.85	0.28	0.06
Ni I	7	5.11	0.07	-1.11	0.02	0.03
Cu I	1	3.53	0.00	-0.66	0.47	0.00
Zn I	2	3.48	0.15	-1.08	0.05	0.10
Sr I	1	0.94	0.00	-1.93	-0.80	0.00
Sr II	0
Y II	4	1.26	0.26	-0.95	0.18	0.13
Zr I	3	1.60	0.05	-0.98	0.16	0.03
Zr II	0
Ba II	2	0.99	0.04	-1.19	-0.06	0.03
La II	2	-0.02	0.03	-1.12	0.01	0.02
Ce II	2	0.09	0.02	-1.49	-0.36	0.01
Nd II	7	0.58	0.21	-0.84	0.29	0.08
Eu II	1	-0.32	0.00	-0.84	0.29	0.00

3.5.5. Aluminium

There are six aluminium transition lines in our optical spectra. The strongest of these lines occur at 3944 and 3961 Å and are visible in all of our stars. However this is a particularly crowded spectral region: the lines fall between the strong Ca H and K lines, with the 3961 Å transition clearly located in the wing of the Ca H line. This makes the continuum determination and subsequent aluminium measurement non-trivial, especially given the metallicity of our stars. Additionally, the 3944 and 3961 Å lines suffer from appreciable depar-

tures from the assumption of local thermal equilibrium (LTE), resulting in under-estimated abundances by up to ∼0.60 dex (Baumueller & Gehren 1997). Instead, we have measured Al abundances from other available transitions: the Al I lines at 6696, 6698, 7835 and 7836 Å. Although these lines are weaker than the bluer Al I lines, their surrounding regions are uncrowded from strong absorption lines.

Generally the four Al I lines are in reasonable agreement with one another, yielding random scatter of less than 0.05 dex. However, these lines were not always detected in the data. The strength of the lines is noticeably

weakened below a 3σ detection with decreasing metallicity and increasing temperature. For our most metal-poor star, J221821-183424, only a single Al I line was detectable, and so we have adopted a conservative uncertainty of ± 0.10 dex.

3.5.6. Iron-peak Elements (Sc, V, Cr and Mn)

As one expects from supernovae, the Fe-peak elemental abundances exhibit similar trends (Figure 6). The noteworthy exception is chromium, where the median abundance is $[\text{Cr}/\text{Fe}] = -0.08 \pm 0.12$ and varies little with overall metallicity. The number of clean, suitable Cr I lines available between candidates fluctuated from three to twelve. Very little line-to-line scatter is present in both Cr I and II: the random scatter is below 0.04 dex for most stars, with the isolated example of J223504-152834 where $\sigma([\text{Cr II}/\text{Fe}]) = 0.29$ dex, and only three lines were available. The Cr I and II mean abundances for J223504-152834 are in good agreement (0.05 dex), and since none of the measured Gaussian profiles appeared particularly unusual, we chose not to exclude any measurements. For all other stars, the $(\text{Cr I} - \text{Cr II})$ abundance differences varied between 0.02 dex up to 0.31 dex. The largest discrepancy occurred in our hottest star, where fewer chromium transitions were measurable. Chromium abundances are only available for one of the standard stars, where our $[\text{Cr}/\text{Fe}] = 0.03$ dex is in excellent agreement with Fulbright (2000), where they find $[\text{Cr}/\text{Fe}] = 0.04$ dex.

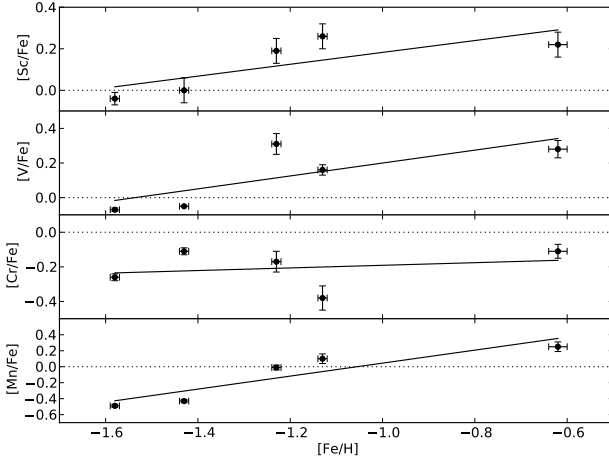


FIG. 6.— Iron peak element abundances (Sc, V, Cr, and Mn) with respect to iron for all Aquarius stream stars.

All other iron peak elements considered (Sc, V, Mn) all exhibit a slight downward trend in metallicity, with manganese demonstrating the strongest gradient: varying between $[\text{Mn}/\text{Fe}] = -0.52$ dex to $+0.31$ dex in the most metal-poor and -rich stars respectively. The $[\text{Sc}/\text{Fe}]$ measurements presented in Figure 6 are calculated from six clean Sc II lines, and there is very minimal line-to-line scatter, the largest of which is 0.06 dex. Three Aquarius stream stars exhibit $[\text{Sc}/\text{Fe}] \sim +0.20$, while J221821-183424 and J223811-104126 have $[\text{Sc}/\text{Fe}] = 0.01$ and 0.05 dex, respectively.

3.5.7. Nickel

Most Aquarius stream stars have seven clean Ni I transitions available. These lines are in excellent agreement, with typical scatter of 0.03 dex. Nickel abundances have been published for two of our standard stars: HD 76932 (Fulbright 2000) and HD 141531 (Shetrone 1996). In both cases, our $[\text{Ni}/\text{Fe}]$ abundance ratios are slightly higher by 0.08 and 0.10 dex respectively. The different solar compositions employed by this study accounts for 0.01 dex. While our nickel abundances may be slightly over-estimated, this does not affect our conclusions.

3.6. Neutron-capture Elements

Neutron-capture elements (Sr to Eu; $38 \leq Z \leq 63$) can be forged through multiple nucleosynthetic processes. The two primary processes that produce these elements are the rapid (r -) process and the slow (s -) process. While the r -process occurs primarily from SN explosions, the s -process takes place foremost in AGB stars. Measurable neutron-capture elements in our spectra are discussed separately.

3.6.1. Strontium, Yttrium and Zirconium

These weak s -process elements generally change in lock-step with one another. Of Sr, Y and Zr, yttrium has the highest number of clean measurable transitions in our wavelength range. The Sr II lines at 4077 and 4215 Å were not measurable in any program or standard stars, although Sr I was detectable at 6645 Å. While $[\text{Y II}/\text{Fe}]$ and $[\text{Zr I, II}/\text{Fe}]$ are in good agreement in all candidates, $[\text{Sr I}/\text{Fe}]$ is lower and there is significant scatter. No obvious telluric contamination was observed in the 6645 Å line. Given that Sr I transitions are susceptible to non-LTE effects (Hansen et al. 2013), we note these Sr abundances should be treated with some caution.

This is the first study to present Sr, Y, and Zr abundances for five of the six standard stars. Existing data on neutron-capture abundances were not crucial in selecting standard comparison stars, it was more important to cover a range of stellar parameters.

The Aquarius candidates have yttrium abundances consistent with halo field stars, with the exception of C222531-145437. With $[\text{Y}/\text{Fe}] = 0.79$ dex, C222531-145437 is significantly overabundant in yttrium for its metallicity (see Figure 4 of Travaglio et al. 2004). The closest star with a similar overabundance in yttrium is the a metal-poor dwarf HD 23439 with $[\text{Y}/\text{Fe}] \sim 0.60$ dex. C222531-145437 is consistently over-abundant in Sr and Zr, too. All other program and standard stars have s -process trends and abundances that are consistent with the chemical evolution of the Milky Way.

3.6.2. Barium and Lanthanum

Barium is primarily produced through the s -process, and its measurement requires some careful consideration. The strong resonance lines at 4554 Å and 4934 Å have appreciable hyperfine splitting, which can result in over-estimated abundances if unaccounted for. There are a few singly ionised lines available in our spectra that do not suffer from strong hyperfine splitting, namely the 5853, 6141 and 6496 Å transitions. Depending on the radial velocity of the star, sometimes our 6496 Å line was

affected by small amounts of telluric absorption. In these cases the line was discarded. The abundances tabulated in Table 6 are based on the remaining clean Ba II lines at 5853 and 6141 Å, which are generally in good agreement with each other, and the 6496 Å line when it was not affected by Earth's atmospheric absorption.

Our standard stars have [Ba/Fe] abundances very typical of the Milky Way halo. Two of the standard stars have published [Ba/Fe] abundance ratios from high-resolution spectra: HD 44007 and HD 76932. We find HD 44007 to have $[{\rm Ba}/{\rm Fe}] = -0.05 \pm 0.04$, which is near the mid-point of existing published measurements from Fulbright (2000) and Burris et al. (2000) of -0.27 and 0.05 dex, respectively. For HD 76932 our measurement of $[{\rm Ba}/{\rm Fe}] = 0.03$ is in good agreement with the Fulbright (2000) value of -0.02 , especially so when differences in adopted solar composition are considered.

With one exception, the Aquarius stream candidates have barium abundances that are quite similar to the stellar halo, ranging between $[{\rm Ba}/{\rm Fe}] = -0.02$ to 0.15 dex. The exception – again – is C222531-085103, which has an anomalously high barium abundance of $[{\rm Ba}/{\rm Fe}] = 0.62$ dex. This is ~ 0.60 dex higher than the Milky Way trend at its given metallicity of $[{\rm Fe}/{\rm H}] = -1.26$ dex. Our three Ba II lines in C222531-085103 are in excellent agreement with each other: 0.64, 0.61, and 0.68 dex. The 6496 Å transition in C222531-085103 has a negligible telluric contribution and was included for this candidate.

3.6.3. Cesium, Neodymium and Europium

Europium abundances have been determined from the equivalent widths of the 6645 Å Eu II transition and synthesis of the region surrounding the 6437 Å Eu II feature. As pointed out by Lawler et al. (2001), the 6437 Å feature is appreciably blended by a silicon line at 6437.71 Å. Measurements of the two lines were consistent with a hidden blend: the 6437 Å Eu II line abundance from equivalent widths was systematically higher than the 6645 Å counterpart. As with other heavy elements except for europium, candidate C222531-145437 is over-abundant in cesium and neodymium with respect to the rest of the sample. We note that in our most metal-poor star the two Eu II lines were wildly discrepant. Neither profile seemed ill-fitted, so we kept both and accepted an extremely large uncertainty for this measurement.

3.7. Distances

Many groups have determined distances for stars in the RAVE survey catalog, which includes all known Aquarius members. Williams et al. (2011) tabulated a range of distances inferred by different techniques. Not every measurement approach was applicable to all stream members. The reduced proper motion distance technique was the only method to infer distances for all Aquarius candidates. The variations between distance measurements for the same star were large. In particular the distance for C222531-146537 ranged from 1.4 ± 0.1 kpc (Burnett & Binney 2010) to 10.3 ± 2.4 kpc (Breddels et al. 2010), where both groups claim to have the ‘most likely’ distances.

Using the stellar parameters tabulated in Table 3, we have calculated distances by isochrone fitting. The Dot-

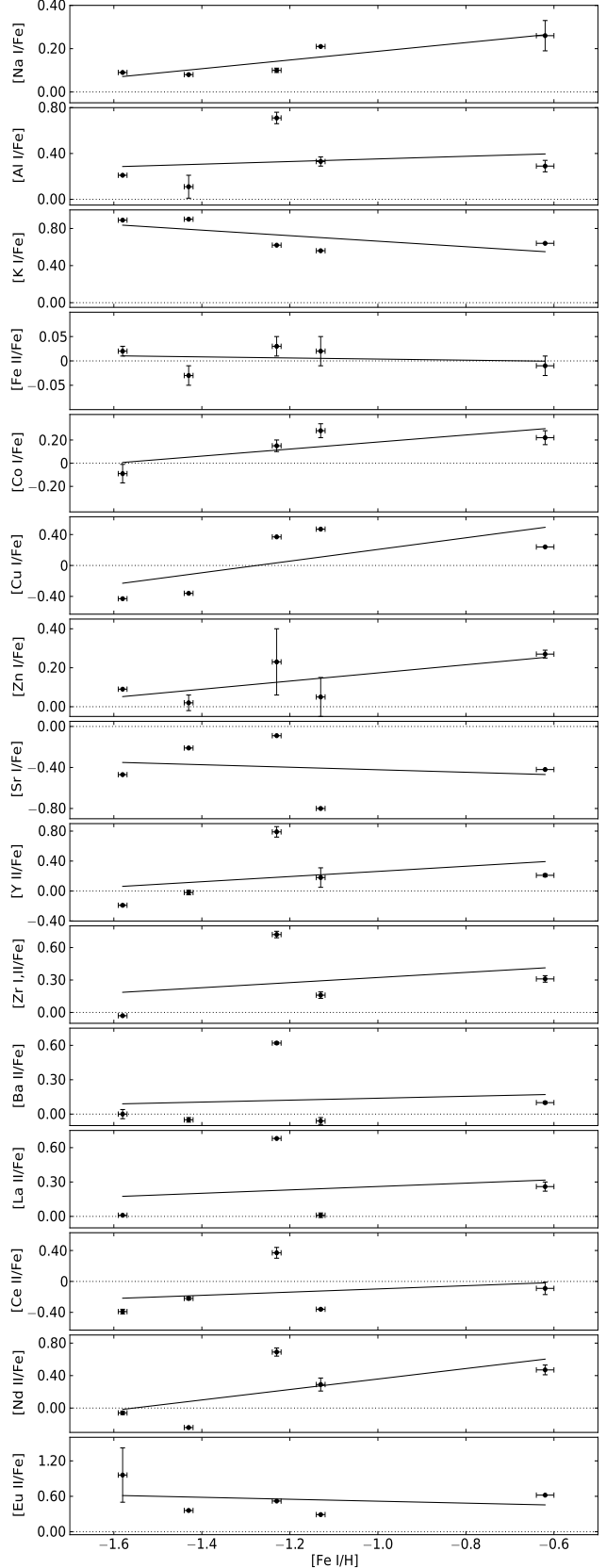


FIG. 7.— Element ratios for Aquarius stream candidates. In the case of $[{\rm Zr}/{{\rm Fe}}]$, $[{\rm Zr}\,{\rm I}/{{\rm Fe}}]$ is taken where available and $[{\rm Zr}\,{\rm II}/{{\rm Fe}}]$ if no measurement was available for ${\rm Zr}\,{\rm I}$. See Table 6 for details.

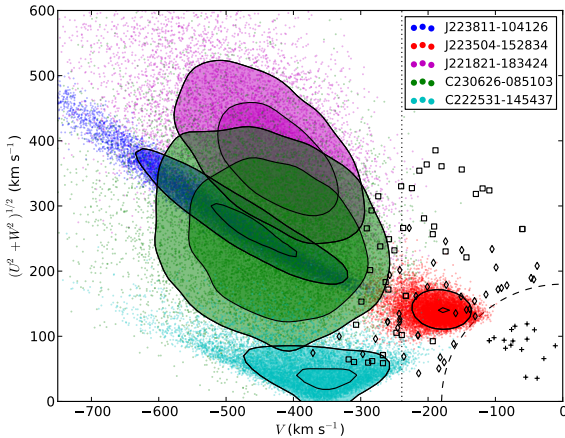


FIG. 8.— Galactic plane rotational velocities versus out-of-plane total velocities. The contours of each star represent the 68% and 95% confidence intervals from 10,000 Monte-Carlo realisations of the parameter distributions shown in Table 7. A sample of thick disc data from Nissen & Schuster (2010) is shown (+), as well as their high- and low-alpha halo populations (\diamond and \circ respectively).

ter et al. (2008) alpha-enhanced ($[\alpha/\text{Fe}] = +0.4 \text{ dex}$) isochrones were employed for these calculations, and an age of 10 Gyr was assumed for all stars. The closest point to the isochrone was found by taking the uncertainties in T_{eff} and $\log g$ into account and measuring the distance modulus in J band. Given the number of uncertain measurements involved in calculating distances (T_{eff} , $\log g$, E(B-V), J) and resulting asymmetric uncertainties, distances were determined from 10,000 Monte-Carlo realisations. For the case of J223811-104126, the extinction of $E(B - V) = 0.12^{+0.01}_{-0.02}$ as from the interstellar Na D1 line has been used. Table 7 shows the parameters and uncertainties adopted for the Monte-Carlo realisations. Uncertainties in parameters were assumed to be Gaussian. The emergent distances and asymmetric uncertainties are also tabulated. Of the distance scales collated in Williams et al. (2011), our distances are in most agreement with the Zwitter et al. (2010) system. In fact, we find the best agreement with the mean of all the distance scales tabulated in Williams et al. (2011). The uncertainties in our distance determinations are on the order of twenty percent.

3.8. Dynamics

Velocity vectors and galactic orbits have been determined in the same Monte-Carlo realisations outlined in Section 3.7. Uncertainties in distance, proper motions⁷ and heliocentric velocity have been propagated. We assumed zero uncertainty in on-sky projected position (α, δ). Orbital energy calculations have assumed a three-component model (bulge, disc, halo) of the galactic potential that reasonably reproduces the galactic rotation curve. The bulge is represented by a Hernquist potential:

$$\Phi_{\text{bulge}}(x, y, z) = \frac{GM_b}{r + a} \quad (2)$$

⁷ The proper motions in Table 1 of Williams et al. (2011) are mis-associated to incorrect stars. This error was typographical; it did not affect the transverse velocity calculations (M.E.K. Williams, private communication). The proper motions listed in our Table 7 are correct.

where $a = 0.6 \text{ kpc}$. The disc is modelled as a Miyamoto-Nagai potential (Miyamoto & Nagai 1975) where:

$$\Phi_{\text{disc}}(x, y, z) = \frac{GM_{\text{disc}}}{\sqrt{x^2 + y^2 + (b + \sqrt{z^2 + c^2})^2}} \quad (3)$$

with $b = 4.5 \text{ kpc}$ and $c = 0.25 \text{ kpc}$ and the galactic halo is represented by a Navarro-Frenk-White dark matter halo (Navarro et al. 1997):

$$\Phi_{\text{halo}} = -\frac{GM_{\text{vir}}}{r [\log(1 + c) - c/(1 + c)]} \log\left(1 + \frac{r}{r_s}\right) \quad (4)$$

with the three components scaled such that the disc provides 85% of the radial force at R_{\odot} , in order to yield a flat circular-speed curve at R_{\odot} . The solar motion of Schönrich (2012) has been assumed where $R_{\odot} = 8.27 \text{ kpc}$ and circular velocity speed of $V_c = 238 \text{ km s}^{-1}$.

Orbital energies and angular momenta from Monte-Carlo simulations are illustrated in Figure 9. The 16,686 stars from the Geneva-Copenhagen Survey sample (Nordström et al. 2004) are also shown as a reference, which primarily consists of nearby disc stars. The Aquarius stream members have bound orbits, all of which are probably retrograde with the exception of J223504-152834. The chemically distinct star, C222531-145437, has a much lower velocity out of the plane ($\sqrt{U^2 + W^2}$) and has an orbit that is more tightly bound to the Milky Way than the other Aquarius members.

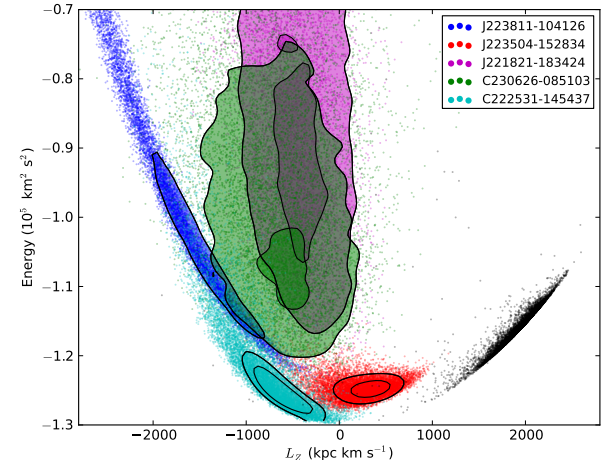


FIG. 9.— A Linblad ($L_Z - E$) diagram showing angular momenta and orbital energies after 10,000 Monte-Carlo realisations for each Aquarius stream star. Iso-contours represent the 68% and 95% confidence intervals. The black points without contours are from the Geneva-Copenhagen Survey sample (Nordström et al. 2004), which primarily consists of nearby disc stars and serves as a validation of our orbital energy calculations.

4. DISCUSSION

4.1. Stellar Parameter Discrepancies with Wylie-de Boer et al. (2012)

We seek to investigate the nature of the Aquarius stream, as well as the specific globular cluster origin claim made by Wylie-de Boer et al. (2012). The stellar parameters reported in Wylie-de Boer et al. (2012)

TABLE 7
PARAMETERS AND UNCERTAINTIES ADOPTED FOR MONTE-CARLO REALISATIONS

Designation	T_{eff} (K)	$\log g$ (dex)	J (mag)	$E(B - V)$ (mag)	D (kpc)	V_{hel} (km s $^{-1}$)	μ_{α} (mas yr $^{-1}$)	μ_{δ} (mas yr $^{-1}$)
C222531-145437	4365 ± 150	1.25 ± 0.30	10.341 ± 0.022	0.03 ± 0.01	$5.1^{+1.1}_{-0.8}$	-156.4 ± 0.1	3.5 ± 2.1	-14.7 ± 2.2
C230626-085103	4225 ± 150	0.85 ± 0.30	10.312 ± 0.025	0.05 ± 0.01	$6.5^{+1.4}_{-1.1}$	-221.1 ± 0.1	-2.5 ± 2.8	-15.4 ± 2.7
J221821-183424	4630 ± 150	0.88 ± 0.30	10.340 ± 0.021	0.03 ± 0.01	$5.6^{+1.3}_{-0.9}$	-159.5 ± 0.1	-10.6 ± 2.5	-19.3 ± 2.5
J223504-152834	4650 ± 150	2.16 ± 0.30	10.363 ± 0.025	0.04 ± 0.01	$1.9^{+0.5}_{-0.4}$	-169.7 ± 0.1	15.9 ± 2.2	-12.8 ± 2.2
J223811-104126	5190 ± 150	2.93 ± 0.30	10.420 ± 0.018	$0.12^{+0.01a}_{-0.02}$	$1.1^{+0.3}_{-0.2}$	-235.7 ± 0.1	-25.3 ± 2.1	-99.5 ± 2.1

^aExtinction measured directly from interstellar Na D1 line

differ to those published in Table 3. Wylie-de Boer et al. (2012) deduce their stellar parameters by minimizing the χ^2 difference between the observed spectra and synthetic spectra from the Munari et al. (2005) spectral library. The synthetic library has a slightly lower resolution than the observations. The observed spectral range was 4120 to 6920 Å, and the regions used for χ^2 minimisation were 4900–5200 Å and 5575–5725 Å. In general, temperatures between the two studies agree within the uncertainties. Given temperature has the principal effect on spectral features, this is perhaps unsurprising. The only aberration is J223811-104126, where we find an effective temperature of 5190 K, ~ 450 K cooler than the 5646 K found by Wylie-de Boer et al. (2012). Similarly, Williams et al. (2011) report a hotter effective temperature of 5502 K from low-resolution spectra. This is the largest discrepancy we see in any of our standard or program stars.

Photometric temperatures only lend marginal weight towards our spectroscopic temperatures. If the Schlegel et al. (1998) dust maps are employed, then the Alonso et al. (1999) and Casagrande et al. (2010) relations estimate the effective temperatures to be between 5104 K and 5367 K. Our spectroscopic temperature of 5190 K is in excellent agreement with the Alonso et al. (1999) prediction, but not in strong disagreement with the Casagrande et al. (2010) relation either. If we employ the reddening of $E(B - V) = 0.12$ that we have determined from the interstellar Na D1 line, the photometric temperature increases slightly by ~ 100 K, in perfect agreement with the Alonso et al. (1999) scale. We find the surface gravity for J223811-104126 to be 3.00 ± 0.50 dex, placing this star at the base of the red giant branch. Thus, if J223811-104126 is a giant star, our spectroscopic temperatures should be in slightly better agreement with the Alonso et al. (1999) scale, rather than the Casagrande et al. (2010) dwarf/sub-giant scale. However, Williams et al. (2011) and Wylie-de Boer et al. (2012) find this star to be a sub-giant, with a surface gravity $\log g = 4.16$ and 4.60 dex respectively. The Williams et al. (2011) and Wylie-de Boer et al. (2012) temperatures are 150 K and 300 K hotter than the Casagrande et al. (2010) prediction respectively. If our interstellar extinction value is employed – and the star is a sub-giant – then the Williams et al. (2011) and Casagrande et al. (2010) temperatures are in good agreement, but the Wylie-de Boer et al. (2012) measurement is still 175 K cooler.

As a test, we set the temperature for J223811-104126 to be 5600 K – within the temperature regime reported by Williams et al. (2011) and Wylie-de Boer et al. (2012). The slopes in abundance

with excitation potential and reduced equivalent width were large ($m_{\text{Fe I}} = -0.099$ dex eV $^{-1}$, 0.162 dex, $m_{\text{Fe II}} = -0.133$ dex eV $^{-1}$, -0.033 dex respectively), and in doing so we could not find a representative solution for this temperature. Thus although photometric temperatures do not completely resolve this discrepancy in spectroscopic temperatures between this study and others, the Alonso et al. (1999) scale is in good agreement with our spectroscopic temperature if our interstellar extinction value is employed.

In the Wylie-de Boer et al. (2012) study, the surface gravity was determined during the χ^2 minimisation process. Again, with the exception of J223811-104126, our surface gravities are largely in agreement. The only other noteworthy difference in surface gravity is for J221821-183424, where we find a lower gravity of $\log g = 0.88 \pm 0.30$ and Wylie-de Boer et al. (2012) find $\log g = 1.45 \pm 0.35$ dex. Given the difference in the S/N ratio between these studies, this difference is not too concerning.

Wylie-de Boer et al. (2012) calculate microturbulence from empirical relationships derived by Reddy et al. (2003) for dwarfs and Fulbright (2000) for giants. These relationships are based on the effective temperature and surface gravity. Our published microturbulent velocities agree excellently with the values presented in Wylie-de Boer et al. (2012), again with the exception of J223811-104126, where the difference in v_t is directly attributable to the offsets in other observables.

Of all the stellar parameters (T_{eff} , $\log g$, v_t and [M/H]), the metallicities between our two studies vary the most. Here we discuss the potential causes for these discrepancies. In the Wylie-de Boer et al. (2012) study, after the stellar parameters (T_{eff} , $\log g$, v_t , and an initial [M/H] estimate) had been determined through a χ^2 analysis, the authors synthesised individual Fe I and II lines using MOOG. Castelli & Kurucz (2003) stellar atmosphere models were employed (K. Freeman, private communication, 2013) – the same ones used in this study – albeit the interpolation schemes will have subtle differences. The median abundance of Fe I lines was taken as the overall stellar metallicity, scaled using the Grevesse & Sauval (1998) solar composition.

The study of Wylie-de Boer et al. (2012) is of slightly lower resolution ($\mathcal{R} = 25,000$ compared to $\mathcal{R} = 28,000$ presented here), but with a much lower S/N ratio: ~ 25 pixel $^{-1}$ compared to >100 pixel $^{-1}$ achieved here. Given the slightly lower spectral resolution, modest S/N and smaller spectral coverage in the Wylie-de Boer et al. (2012) study, there are fewer unblended absorption lines

available. In fact, there are very few transitions present in their published line list: a maximum of 14 Fe I lines and 3 Fe II lines were available. For contrast, our metallicity determinations are based from 63 Fe I and 13 Fe II clean, unblended lines. Given the metallicity of these candidates and the reasonable wavelength coverage of the Wyylie-de Boer et al. (2012) data, it is somewhat surprising that there were not more transitions available for analysis.

The line list employed in the Wyylie-de Boer et al. (2012) utilised different oscillator strengths than those tabulated in Table 2. The oscillator strengths in the Wyylie-de Boer et al. (2012) study are astrophysical; they were derived from a reverse analysis from the Hinkle et al. (2003) solar atlas. Suspecting the differing line lists may contribute to the metallicity discrepancy, we re-analysed our data using the Wyylie-de Boer et al. (2012) line list and stellar parameters. Indeed, in doing so we arrive at reasonably similar metallicities to Wyylie-de Boer et al. (2012). Without using their published stellar parameters a priori, in a ‘blind’ analysis employing just the Wyylie-de Boer et al. (2012) line list, we also arrive at similar stellar parameters. However, given the limited number of lines available, extremely subtle changes to the stellar parameters inflicted large variations to both the individual and mean Fe abundances. Additionally, we note that one Fe I transition at 6420.060 Å in the Wyylie-de Boer et al. (2012) line list was either not detected at the 3σ level – even though the S/N at this point exceeds 115 pixel $^{-1}$ in every observation – or it was blended with a stronger neighbouring transition. Thus, for this comparative analysis a maximum of 13 Fe I and 3 Fe II lines were available.

Given the line list employed in the Wyylie-de Boer et al. (2012) study, the overall data quality and the lack of suitable iron lines available for analysis, it appears the Aquarius stream stars conspired to present a tight metallicity distribution of $\sigma(\text{Fe/H}) = 0.10 \text{ dex}$. When viewed in light of enhanced [Ni/Fe], [Na/Fe] abundance ratios, this chemistry might be suggestive of a globular cluster origin. Our analysis of high-resolution spectra with high S/N reveals a much broader metallicity distribution for the stream. With just five stars we find the stream metallicity varies from $[\text{Fe/H}] = -0.63$ to -1.63 dex . Although this is a small sample, we find the calculated mean abundance and standard deviation to be $[\text{Fe/H}] = -1.24 \pm 0.36 \text{ dex}$.

4.2. The Aquarius Stream M.D.F.

Classical globular clusters typically exhibit very little chemical scatter. This is largely because they are primarily – and somewhat incorrectly – considered to be a single stellar populations, originating from a lone, largely homogenous proto-stellar cloud. Observations have demonstrated that this is not always the case: many globular clusters clearly host multiple stellar populations. The separation between these sub-populations is identifiable through chemical abundances, and often from photometry alone. One prominent example is that of ω -Centauri (NGC 5139), which is seen to host many sub-populations with very different metallicity distributions. Without the explanation of multiple sub-populations in mind, such a system would be seen to exhibit an unreasonably wide

metallicity dispersion for a single stellar population.

Assuming all our candidates are stream members, we find a metallicity dispersion of $\sigma([\text{Fe}/\text{H}]) = 0.36 \text{ dex}$. If the stream is the result of a disrupted system, this metallicity dispersion provides little indication on the host. If the dispersion were smaller, confirming the observations of Wyylie-de Boer et al. (2012), a globular cluster scenario may be more likely. However, given the multiple stellar populations present in many globular clusters, which can exhibit total cluster dispersions up to X dex (NGC X), Y dex (NGC Y) – hi Gary :-) –, our dispersion of 0.36 dex is somewhat inconvenient. Since dSph galaxies do not undergo chemical self-enrichment in the same way as globular clusters, they can exhibit significant metallicity dispersions – well over a dex, depending on the total system luminosity. On its own, the metallicity of our stream stars does not provide any indication on the cause of the Aquarius stream, or its enrichment environment.

4.3. The Na-O Relationship

Extensive studies looking at stars in globular clusters have revealed variations in light-element abundances, most notably an anti-correlation in sodium and oxygen content (Norris & Da Costa 1995; Carretta et al. 2009, and references therein). This chemical pattern has been repeatedly demonstrated in every well-studied globular cluster, although the strength of the anti-correlation varies in each system. Between generations of stars within a globular cluster, oxygen is converted into nitrogen, thereby reducing the overall oxygen abundance. Even though oxygen undergoes internal mixing during its evolution along the giant branch, the detection of this chemical pattern in unevolved stars led to the conclusion that observed abundance variations due to mixing are limited to lithium, carbon and nitrogen. Therefore, the light element anti-correlation requires a different astrophysical explanation.

Sodium is primarily produced through carbon burning in massive stars by the dominant $^{12}\text{C}(^{12}\text{C}, p)^{23}\text{Na}$ process. The final Na abundance is dependent on the neutron excess of the star, which slowly increases during carbon burning due to weak interactions (Arnett & Truran 1969). Massive stars ($> 8M_{\odot}$) eventually deliver their manufactured sodium to the interstellar-medium through Sn II events. Because the eventual Sn II explosion is devoid of any significant beta-decay processes, the neutron excess of the exploded material is representative of the pre-explosive abundance.

The explosive material eventually condenses to form the next generation of stars, which will have a net increase in their neutron excess with respect to their predecessors. Since the Na-production rate is correlated with the neutron excess, an overall increase in the total sodium content and Na-production rate between stellar generations is expected. Thus, an increase in the sodium abundance between generations of massive stars is a natural consequence of nucleosynthesis. Sodium content also becomes important for production of nickel during the Sn II event (see Section 4.5) because ^{23}Na is the only stable isotope produced in significant quantities during the C- or O-burning stages. A small fraction of ^{22}Na is also forged through proton capture on ^{21}Ne in the carbon shell, an effect which is enhanced by neutrinos spallating abun-

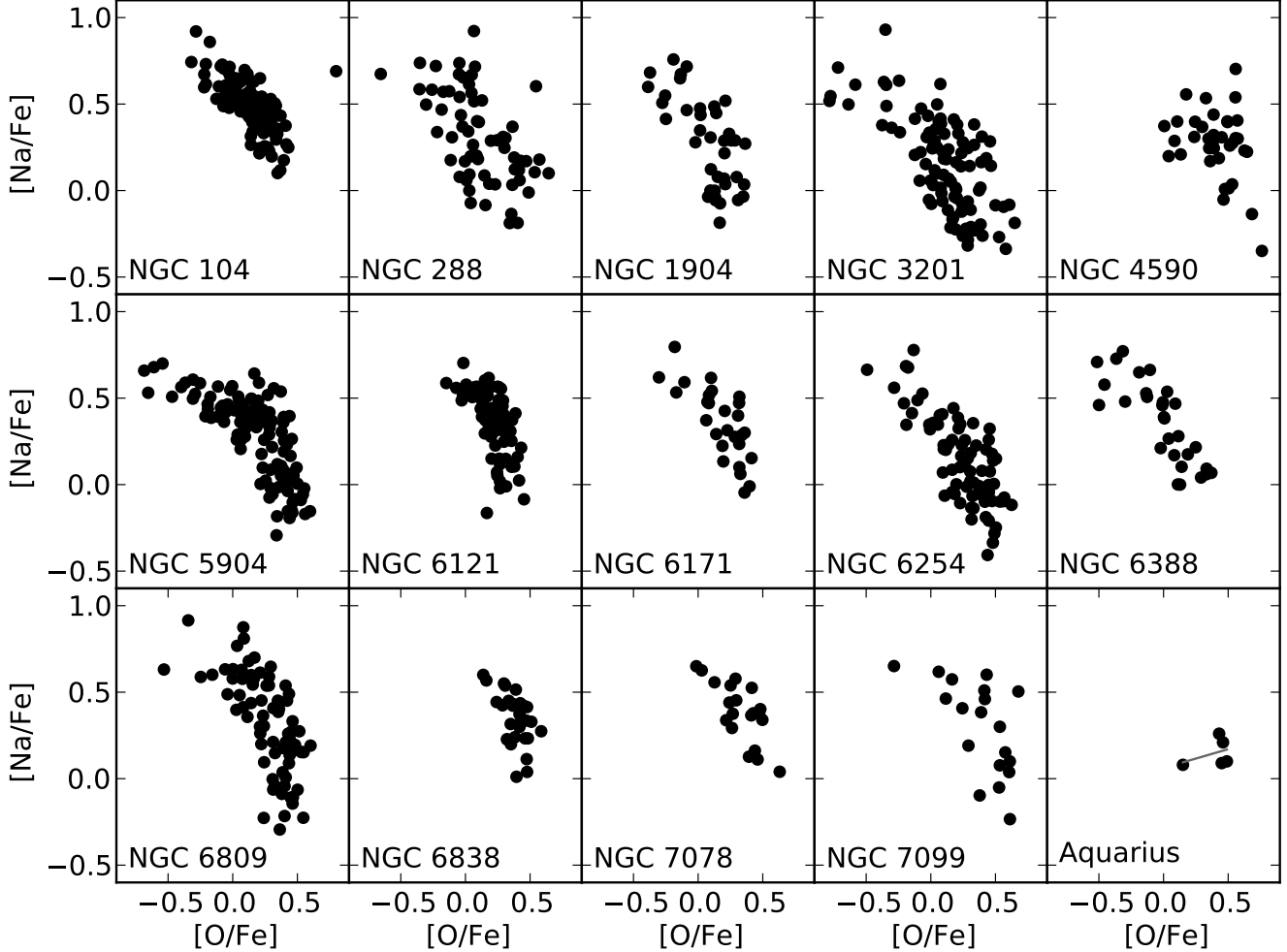


FIG. 10.— Oxygen and sodium abundances for 14 classical globular clusters from Carretta et al. (2009), demonstrating the clear inverse Na-O correlation, ubiquitous to all well-studied globular clusters. The [O/Fe] and [Na/Fe] abundances from this study for the five Aquarius stream candidates are also shown (last panel).

dant elements like ^{16}O and ^{20}Ne , making free protons available for capture (Woosley & Weaver 1995).

Oxygen depletion is likely the result of complete CNO burning within the stellar interior. The nucleosynthetic pathways that produce the Na-O anti-correlation are well known. However, the temperatures required to produce these patterns are not expected within the interiors of globular cluster stars. While the exact mechanism for which these conditions occur remains under investigation, we can describe the abundance variation as a simple oxygen depletion (or dilution) model with time. Through comparisons with existing globular clusters, we can still make inferences on the star-formation history of a system by measuring sodium and oxygen abundances in a sample of its stars.

Carretta et al. (2009) defined three components of stars exhibiting an inverse Na-O correlation within a population: primordial, intermediate, and extreme components. The [Na/Fe] and [O/Fe] abundances for a given star define which component it belongs to. Primordial (first-generation) stars are those with sodium and oxygen abundances which are similar to field stars of the same metallicity. An intermediate component – the second-generation of stars – will have super-solar

sodium abundances and demonstrate a slight depletion in oxygen content. The oxygen exhaustion rate is ultimately dependent on the star-formation history of the cluster environment. The intermediate population is subdivided based on how much the sodium and oxygen abundances depart from the primordial population: stars with $[\text{O}/\text{Na}] > -0.9$ dex are classified as belonging to an extreme component of this Na-O pattern because they differ greatly from the primordial cluster abundance. The extreme O-depletion component has only been observed in a few clusters (preferentially more massive clusters with extended horizontal branches), indicating an long-lasting star-formation history in more massive clusters.

It is clear that careful consideration must be given when inferring star-formation histories from observed stellar abundances. In addition to the normal care afforded for measuring elemental abundances from high-resolution spectroscopic data, attention must be given to telluric absorption, contamination from nickel transitions, as well as non-LTE and 3D effects when determining oxygen abundances. Furthermore, when characterising the oxygen depletion rate – the strength of the Na-O anti-correlation in a given cluster – it is vital to sample stars belonging to all three components, where possible.

If only a primordial sample of stars in a globular cluster is observed, their [Na/Fe] and [O/Fe] abundances will be indistinguishable from field stars of a similar metallicity. In such a scenario, any inferred anti-correlation could equally be explained by intrinsic chemical scatter or observational uncertainties.

Wylie-de Boer et al. (2012) measured sodium and oxygen abundances for four of their six Aquarius stream members. This research has four stars in common with the Wylie-de Boer et al. (2012) study, but sodium and oxygen measurements exist for only three stars intersecting both samples, as the data quality for J223811-104126 in the Wylie-de Boer et al. (2012) was such that it prohibited oxygen determination. We have sodium and oxygen abundances for all of our stars, including J223811-104126, for which we ascertained a conservative upper limit from the [O I] lines of $[O/Fe] < 0.5$ dex, and a abundance ratio of $[O/Fe] = 0.14 \pm 0.08$ from the O I triplet lines. In Figures 10 and 11 we have plotted theses abundances, including the corrected value for J223811-104126 rather than the upper limit.

The Wylie-de Boer et al. (2012) measurements indicate two stars with solar levels of [Na/Fe] – identical to field star abundances for their metallicity – and two stars with enhanced sodium content: J223504-152834 and J232619-080808. We also find J223504-152834 to be sodium-enhanced, whereas the second star in their study, J232619-080808, is not in our sample. We find the additional star not present in the Wylie-de Boer et al. (2012) sample, C2306265-085103, to be sodium enhanced to almost the same level of J223504-152834 with $[Na/Fe] = 0.26$ dex. The sodium-enhanced stars exhibit no depletion of oxygen; their chemistry does not demonstrate a Na-O anti-correlation.

If the Aquarius stream is the result of a disrupted globular cluster, a large part of the picture must still be missing. Almost all of the Aquarius stream stars studied to date (either in this sample or the Wylie-de Boer et al. (2012) study), would be unambiguously classified as belonging to a ‘primordial’ component, with chemistry indistinguishable from the thick disc or halo. Identifying more Aquarius stream members belonging to the intermediate component with strong oxygen depletion, or perhaps members of an extreme component, would be convincing evidence for a Na-O anti-correlation and a globular cluster origin. Three stream stars identified to date (including two from this sample) might arguably be classified as members of an intermediate population, with only a slight enhancement in sodium and no oxygen-depletion. Recall our [Na/Fe] abundance ratios appear systematically higher in our standard stars when compared to the literature. Thus, if the strength of any Na-O relationship is to be used to vet potential disrupted hosts for the Aquarius stream, many more stream members will need to be identified and observed spectroscopically with high-resolution and high S/N . Currently, no evidence exists for a Na-O anti-correlation in the Aquarius stream.

4.4. The Al-Mg Relationship

An inverse relationship between sodium and oxygen is not the only chemical pattern commonly observed in globular clusters. Although not ubiquitous to every system, many clusters exhibit an anti-correlation between

aluminium and magnesium. This is perhaps unsurprising, given the nucleosynthetic pathways for these elements. In addition to the CNO cycle operating during hydrogen burning, the Mg-Al chain can also operate under extreme temperatures ($T_6 \sim 3$ K; Arnould et al. 1999). In these conditions, aluminium is produced by proton capture of magnesium, beginning with ^{24}Mg to ^{25}Al . The lifetime of β -decay to proton capture allows for the production of unstable ^{27}Si through proton capture. Seconds later, the isotope decays to ^{27}Al , completing the ^{27}Si path of the Mg-Al cycle. The alternative process onwards from ^{25}Al involves proton capture to ^{26}Mg , but this process requires much higher temperatures ($T_6 \sim 7$ K). In fact, although the process operates from temperatures above 30 million K, large Mg-Al abundance variations are not appreciable unless the temperatures reach $T_6 \sim 6.5$ K.

The Mg-Al cycle can explain the observed anti-correlation observed in some globular clusters, and most theoretical models predict such a pattern (#get citations from Amanda). However, the locations where these extreme temperatures can be found are under some debate. Theoretical models indicate that the interiors of globular cluster stars do not reach sufficient temperatures for the Mg-Al cycle to produce the observed variations. Thus, although the processes for creating these chemical patterns are understood, the exact site and requisite conditions are lacking a full description.

Wylie-de Boer et al. (2012) published magnesium and aluminium abundances for five stars in their Aquarius sample. No inverse correlation is present in their data, and their abundances are not dissimilar from field stars. Given that we do not find a Na-O anti-correlation, it is not surprising that a Mg-Al pattern is also not observed. The abundances tabulated in Table 6 vary slightly with those presented in the Wylie-de Boer et al. (2012) sample, but we also find no Mg-Al relationship. Two candidates are in good agreement: J221821-183424 and J223811-104126, albeit the data quality in the Wylie-de Boer et al. (2012) study did not permit measuring aluminium for J223811-104126. The other two stars common between studies are C222531-145437 and J223504-152834, which we found to be the most abundant in both magnesium and aluminium.

While Wylie-de Boer et al. (2012) find almost no scatter (± 0.02 dex) in [Mg/Fe] for stars common to both studies, we find C222531-145437 and J223504-152834 to be almost $+0.20$ dex higher than the rest of the sample. C222531-145437 is chemically distinct in other elements, too. The reason for this [Mg/Fe] discrepancy is not obvious, given the stellar parameters between the two studies agree well, with the previously discussed exception of metallicity. In particular, the stellar parameters agree excellently for J223504-152834, but we find $[\text{Fe}/\text{H}] = -0.63$ instead of -0.98 as found by Wylie-de Boer et al. (2012). It is worth noting that our measurement is in between that of Williams et al. (2011) and Wylie-de Boer et al. (2012): Williams et al. (2011) find $[\text{M}/\text{H}] = -0.33$ dex. Of the Mg I profiles measured, only two transitions are common to both line lists: 6318 Å and 6319 Å. The oscillator strengths differ between studies; in these two lines the log gf differs by -0.24 and -0.27 dex respectively (our oscillator strengths are lower). This in-

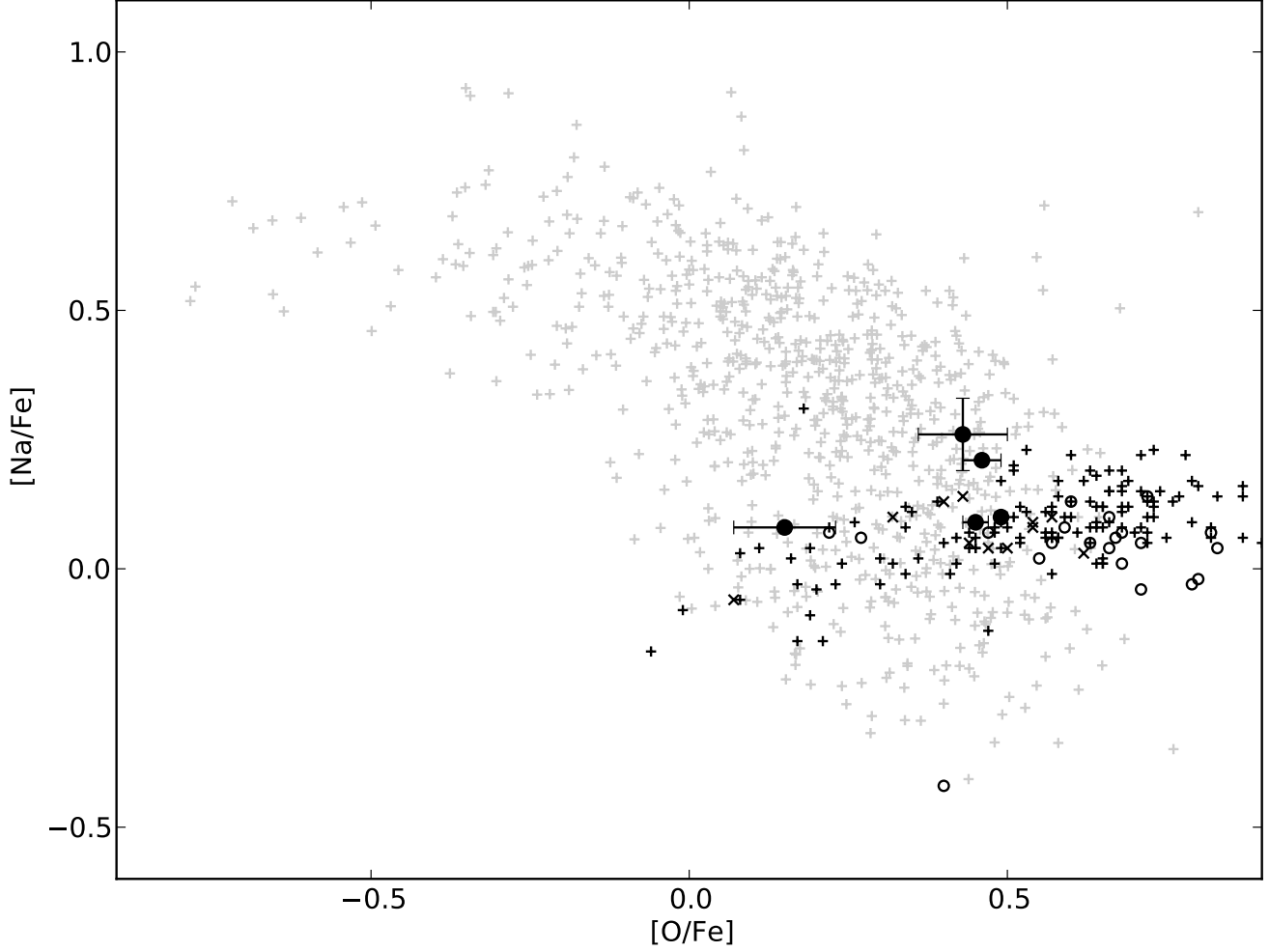


FIG. 11.— Oxygen and sodium abundances for thick disc (+), thin disc (x) and halo (o) stars from Reddy et al. (2006), and globular cluster stars from Carretta et al. (2009) (grey symbols). The Aquarius candidate abundances are also shown (●), illustrating how their [O/Fe], [Na/Fe] content is not dissimilar from galactic stars. Ambiguous thick disc/thin disc stars in Reddy et al. (2006) are marked with thick disc symbols (+), as are uncertain thick disc/halo stars with halo symbols (○).

dicates that the difference in oscillator strengths may explain the ~ 0.2 dex offset in [Mg/Fe] between this study and that of Wylie-de Boer et al. (2012).

The [Mg/Fe] and [Al/Fe] abundances found for the five Aquarius stars in this sample are illustrated in Figure 13. Our stars exhibit a strong positive relationship, with a best-fitting slope of $[Al/Fe] = 2.08 \times [Mg/Fe] - 0.57$, which is in part driven by C222531-145437. If we exclude this chemically peculiar star with enhanced [Al/Fe] relative to the rest of the sample, the slope decreases to $[Al/Fe] = 0.96 \times [Mg/Fe] - 0.16$, a near 1:1 relationship. Even when a Mg-Al anti-correlation is not detected in globular clusters, there is generally more scatter in [Al/Fe] at near-constant [Mg/Fe] (e.g. see Figure 13 or Carretta et al. 2009). To the author’s knowledge of the literature no classical globular clusters exhibit a positive correlation, and nor is it expected in globular clusters.

A positive relationship between magnesium and aluminium can result from Sn II contributions to the local interstellar medium. High-resolution observations of disc stars illustrate this correlation, demonstrating efficient Sn II mixing. Some intermediate-mass ($\sim 4M_{\odot}$) AGB models also contribute towards a positive correlation be-

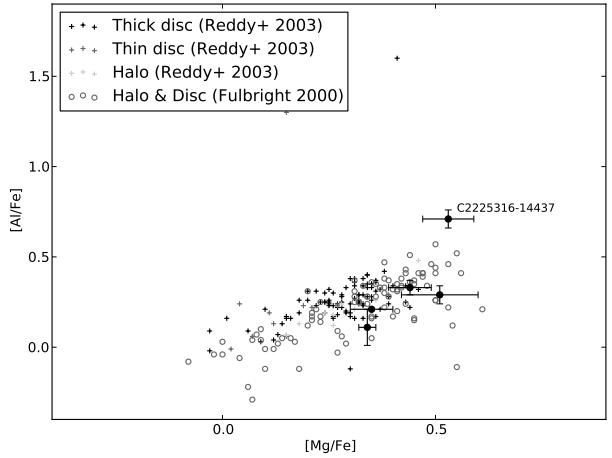


FIG. 12.— Magnesium and aluminium abundances for Aquarius stream candidates (●), and Milky Way halo/disc stars from Reddy et al. (2003) (+) and Fulbright (2000) (○). The chemically peculiar star, C222531-145437, is marked.

tween aluminium and magnesium. Under extreme temperatures ($T_6 \sim 300$ K), substantial ^{25}Mg and ^{26}Mg are

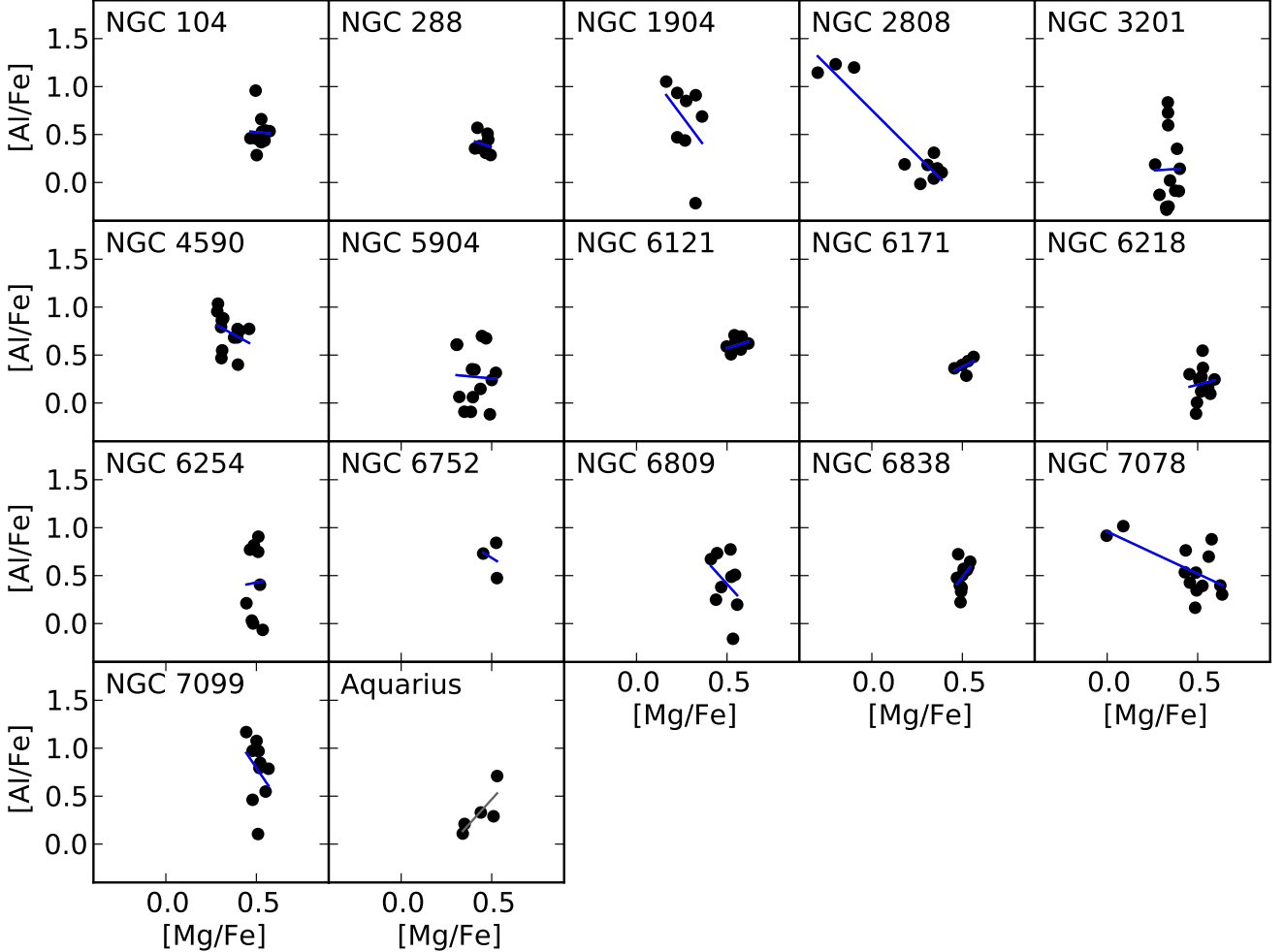


FIG. 13.— $[\text{Mg}/\text{Fe}]$ and $[\text{Al}/\text{Fe}]$ abundances for stars in 16 globular clusters from Carretta et al. (2009) and for the five Aquarius stream candidates. The inverse Mg-Al correlation is illustrated, most obviously in NGC 2808 and NGC 1904. The strong positive correlation observed in Aquarius is in stark contrast with other classical globular clusters.

produced by α -capture onto ^{22}Ne by the $^{22}\text{Ne}(\alpha, \text{n})^{25}\text{Mg}$ and $^{22}\text{Ne}(\alpha, \gamma)^{26}\text{Mg}$ reactions respectively. Following deep dredge up, significant ^{25}Mg and ^{26}Mg is mixed into the photosphere, more so than the quantity of ^{26}Al produced through the Mg-Al cycle. This dredge up process replenishes the Mg that is expended during the Mg-Al pathway. Therefore, a positive relationship between magnesium and aluminium can occur if there has been significant contributions from intermediate mass AGB stars.

An unrealistically high fraction of intermediate-mass AGB stars would be required to produce the same chemical signature of a single Sn II event. Given the efficiency of chemical pollution following supernovae, the observed correlation in the thick disc is likely the result of Sn II events. However, since the chemical enrichment environment of the Aquarius stream is unknown, we cannot exclude either possibility. Distinguishing between these processes observationally requires careful measurements of magnesium isotope abundances ^{24}Mg (indicating supernovae mixing), ^{25}Mg and ^{26}Mg (suggesting significant AGB contribution), which is not possible given our S/N or spectral resolution.

4.5. The Na-Ni Relationship

Detailed chemical studies of nearby disc stars have noted a correlation with $[\text{Na}/\text{Fe}]$ and $[\text{Ni}/\text{Fe}]$ abundance ratios. This relationship was first hinted in Nissen & Schuster (1997), where the authors found eight stars that were under-abundant in $[\alpha/\text{Fe}]$, $[\text{Na}/\text{Fe}]$ and $[\text{Ni}/\text{Fe}]$. Interestingly, the authors noted that stars at larger galactocentric radii were most deficient in these elements. Fulbright (2000) saw a similar signature: stars with low $[\text{Na}/\text{Fe}]$ were only found at large ($R_\odot > 20\text{ kpc}$) distances. Nissen & Schuster (1997) proposed that since the outer halo is thought to have been largely built up by accretion, then the Na-Ni pattern may be a chemical indicator of merger history within the galaxy.

With additional data from Nissen & Schuster (2011), the Na-Ni relationship was found to be slightly steeper than originally proposed. The pattern exists only for stars with $-1.5 < [\text{Fe}/\text{H}] < -0.5$ dex, and is not seen in metal-poor dSph stars, providing a potentially useful indicator for investigating chemical evolution. However, it is crucial to note that although there are only a few dSph stars in the $-1.5 < [\text{Fe}/\text{H}] < -0.5$ metallicity regime with $[\text{Na}/\text{Fe}]$, $[\text{Ni}/\text{Fe}]$ measurements, they agree

reasonably well with the galactic trend.

The correlation between sodium and nickel content is the nucleosynthetic result of neutron capture in massive stars. As previously discussed, the total Na abundance is controlled by the neutron excess, which limits the production of ^{58}Ni during Sn II events. When the inevitable supernova begins, the core photodissociates into neutrons and protons, allowing the temporary creation of ^{56}Ni before it decays to ^{56}Fe . A limited amount of ^{54}Fe is also formed, which is the main source of production for the stable ^{58}Ni isotope through α -capture. When the core dissociates, the quantity of ^{54}Fe (and hence ^{58}Ni) produced is dependent on the abundance of neutron-rich elements during the explosion. As ^{23}Na is a relatively plentiful neutron source with respect to other potential sources (like ^{13}C), the post-supernova ^{58}Ni abundance is driven by the pre-explosion ^{23}Na content. Recall that the total Na production primarily depends on the neutron excess. Thus, through populations of massive stars undergoing C-burning, a positive correlation between sodium and nickel can be expected.

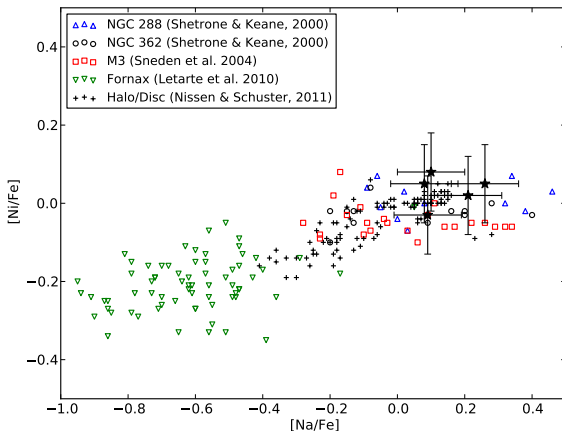


FIG. 14.— [Na/Fe] and [Ni/Fe] for Aquarius stream candidates and for globular cluster, dSph, and field (halo/disc) stars. The Nissen & Schuster (2011) plotted sample included halo stars, ω -low and ω -high disc members. As noted by Nissen & Schuster (1997, 2011), a positive Na-Ni relationship exists for field stars, with dSph members exhibiting strong depletion in both elements and globular cluster stars consistently showing an enhancement. Sodium and nickel content for Aquarius members indicate a dSph accretion origin is unlikely.

Stars originating in dwarf spheroidal galaxies and globular clusters have very different chemical enrichment environments. Consequently, both types of systems exhibit chemistry that reflects their nucleosynthetic antiquity. Dwarf spheroidal stars do not demonstrate enhanced sodium or nickel content with respect to iron, as there has been a relatively small lineage of massive stars undergoing supernova. In contrast, globular cluster stars do have elevated [Na/Fe], [Ni/Fe] signatures. This sharp contrast between dwarf spheroidal and globular cluster star chemistry is illustrated in Figure 14. Given the extended star formation within the Milky Way disc, globular cluster stars and disc stars are indiscernible in the Na/Ni plane: they both show an extended contribution of massive stars. The most that can be inferred from the

Na, Ni abundances of Aquarius stream stars is that their enrichment environment is less like a dSph galaxy, and more representative of either a globular cluster, or the disc of the Milky Way.

4.6. The Distinctiveness of C222531-145437

C222531-145437 exhibits peculiar chemical abundances compared to the rest of the Aquarius candidates. In almost every element with respect to iron, C222531-145437 is distinct from the other Aquarius candidates. It is over-abundant in light refractory elements, weak and heavy *s*-process elements, with a strong barium abundance of [Ba/Fe] = 0.68 dex. This value is well in excess of the halo ([Ba/Fe] \sim 0.0) – and our other Aquarius stream stars – which vary between –0.02 to 0.15 dex.

Although no radial velocity variations were observed between exposures, it is possible that an unseen AGB star has contributed to the surface abundances of C222531-145437. The abundances of heavy elements produced by AGB stars have a high dependence on the overall metallicity and mass of the AGB star. Low-mass ($\lesssim 3M_{\odot}$) AGB stars produce high fractions of heavy *s*-process elements compared to their weak *s*-process counterparts. As such, [Ba/Y] is a useful indicator when considering contributions from a low-mass AGB companion. For C222531-145437, [Ba/Y] = –0.17, which is much lower than expected if a low-mass AGB star was the dominant reason for the heavy element enhancements ([Ba/Y] \sim 0.5). Intermediate-mass ($3\text{-}5M_{\odot}$) AGB stars also cannot explain the abundances for C222531-145437: using recently computed intermediate-mass AGB yields for $3\text{-}5M_{\odot}$ for a star of [Fe/H] = –1.2 (Fishlock, Karakas et al., forthcoming) we find the expected surface abundances do not match the observations. If mass transfer from an AGB companion is ongoing or has occurred very recently, non-negligible amounts of technetium is produced, and remains visible before it decays over \sim 100 Myr[citation needed]. We saw no technetium absorption feature at the 4049.11, 4238.19 or 4297.06 Å wavelengths in the spectrum of C222531-145437. Therefore, we find no reason to suspect the heavy element enhancement in C222531-145437 is the result of an AGB companion.

High *s*-process enhancements have been noted for a few disrupted globular clusters that exhibit a wide metallicity range. Most notably ω -Centauri (Majewski et al. 2012) and M22 (Marino et al. 2011). Like the Aquarius co-moving group, both clusters are relatively close to the sun: R_{\odot} = 5.2 kpc and 3.2 kpc, respectively. M22 has a mean metallicity of [Fe/H] \sim –1.7, varying between $-2.0 < [\text{Fe}/\text{H}] < -1.6$ dex. Since C222531-145437 has a metallicity of [Fe/H] = –1.26 dex, it is unlikely to be associated with M22. However, the high barium content and overall metallicity of C222531-145437 ([Fe/H] = –1.26) suggests there may be an association with ω -Centauri.

ω -Centauri has a retrograde orbit with low inclination. Many groups simulating this orbit have predicted retrograde tidal debris to occur near the Solar circle (Dinescu 2002; Tsuchiya et al. 2003, 2004; Bekki & Freeman 2003). Subsequent searches for ω -Centauri debris in the solar neighbourhood have led to tantalising signatures of debris. From over 4,000 stars targeted by Da Costa & Cole-

man (2008), only six candidate debris members were recovered. More recently, Majewski et al. (2012) presented data from the Grid Giant Star Survey (GGSS), an all-sky search looking for metal-poor giant stars. From their data they identified 12 stream candidates. Although this scarcity is consistent with tidal stripping occurring long ago, it is perhaps worrying that searches for stripped stars closer to ω -Centurai itself have been even less successful.

In addition to presenting new stream candidates, Majewski et al. (2012) performed 4,050 simulations in order to predict likely locations for ω -Centurai tidal debris. The results of their simulation are replicated in Figure 15, where the location of C222531-145437 is also shown. Interestingly, the velocity and position of C222531-145437 line up almost precisely where Majewski et al. (2012) predict a high probability of tidal debris.

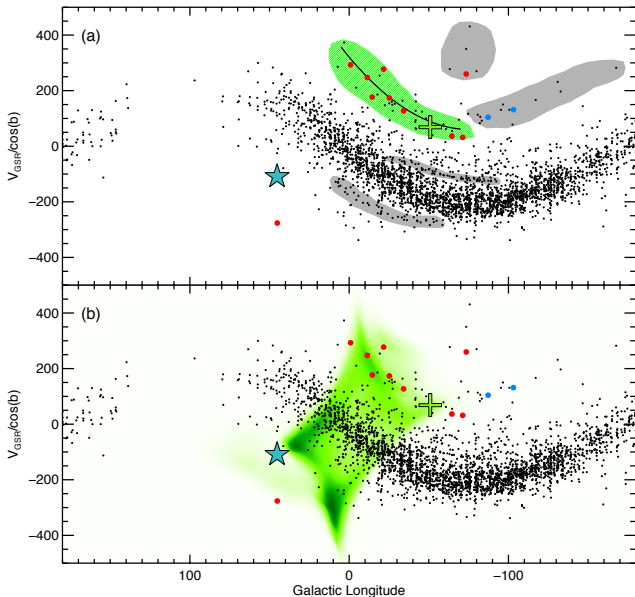


FIG. 15.— Panel (a) shows the distribution of giant stars in the GGSS (Majewski et al. 2012) in galactic longitude and $V_{\text{GSR}}/\cos(b)$ after excluding stars with $|b| > 60^\circ$. Stars from the GGSS sample believed to be ω Cen tidal debris are shown in green shading. Red points are stars from the GGSS sample with abundances that follow the ω Cen $[\text{Ba}/\text{Fe}]$ – $[\text{Fe}/\text{H}]$ pattern. Blue points are those with echelle spectra that do not follow this trend. Grey shading highlights other potential halo substructures from their study. Panel (b) shows the probability distribution of ω Cen tidal debris from 4,050 simulations. The ω Cen core is shown as a green cross and the cyan star represents C222531-145437, falling almost precisely where a relatively high probability of ω Cen tidal debris is expected.

Perhaps the most striking evidence for an association between C222531-145437 and ω -Centurai is in its chemistry. Figure 16 demonstrates the $[\text{Ba}/\text{Fe}]$ abundance for ω -Centurai stars compared to that of the galactic halo. A steep barium enhancement is present, which is unique to the globular clusters ω -Centurai and M22. We note that although high *s*-process enrichment is present in other systems (IC 2391, the Argus association; De Silva et al. 2013), these systems are have metallicities near solar and are unlikely to be associated with C222531-145437. Furthermore, *all other elemental abundances* measured here precisely match with those presented by Marino et al. (2011) for ω -Centurai RGB stars.

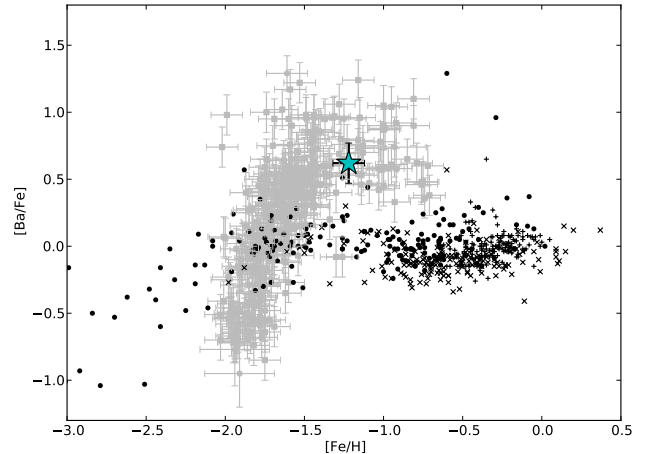


FIG. 16.— $[\text{Fe}/\text{H}]$ and $[\text{Ba}/\text{Fe}]$ for halo/disc stars (black) from Fulbright (2000); Reddy et al. (2003, 2006) and ω -Centurai RGB stars (grey) from Francois et al. (1988); Smith et al. (2000); Marino et al. (2011). Similar trends are observed for other heavy elements in ω -Centurai members. The candidate we associate with ω -Centurai tidal debris, C222531-145437, is marked in cyan.

The chemical peculiarity of C222531-145437 suggests that it is distinct from the Aquarius co-moving group. The high *s*-process enrichment is similar to that observed in ω -Centurai stars, and the overall metallicity ($[\text{Fe}/\text{H}] = -1.26$) agrees excellently with the mean metallicity of a known sub-population within ω -Centurai. Moreover, the position and velocity for C222531-145437 precisely coincide with the most likely predictions for tidal debris from ω -Centurai, and the angular momentum and orbital energy precisely matches those found for ω -Centurai by Dinescu et al. (1999). The chemical and phase-space information indicates that C222531-145437 is clearly associated with the disrupted globular cluster ω -Centurai.

In their original discovery paper, Williams et al. (2011) attempted to exclude possible known progenitors for the Aquarius stream. On the basis of metallicity, distance, proper motions, transverse velocities and orbital energies, the authors were able to exclude all known Milky Way satellites, with the notable exception of ω -Centurai. Although the Aquarius stream metallicity distribution we find is not dissimilar from a known sub-population in ω -Centurai, the individual chemical abundances are quite distinct. The strong *s*-process enhancement with overall metallicity is not observed in the rest of our sample. Thus, with the exception of C222531-145437, the Aquarius members do not have chemistry that is synonymous with ω -Centurai tidal debris.

4.7. Disrupted disc/Halo Stars – Signature of a Disc-Satellite Interaction?

Since the Aquarius stream is kinematically coherent, the default assumption is that the co-moving group has accreted onto the Milky Way from a tidally disrupted satellite. The stream candidates presented here are slightly enhanced in sodium and nickel, suggesting that if a satellite parent ever existed then its chemical enrichment environment was more like a globular cluster than a dSph galaxy. Based on a lack of α -enhancement and increased $[\text{Na}/\text{Fe}]$, $[\text{Ni}/\text{Fe}]$ abundance ratios we exclude the possibility that the Aquarius stream has resulted from a

disrupted dwarf galaxy. If the progenitor is a disrupted globular cluster, and most of our candidates are members, then the parent has a wider metallicity distribution than most globular clusters.

However we find no chemical evidence for a globular cluster origin. If the Aquarius co-moving group is a relic of a disrupted globular cluster then high-resolution, high S/N spectra for the entire stream may be required before chemical patterns reminiscent of classical globular clusters becomes apparent. As it stands, the Aquarius group appears chemically indistinguishable from thick disc/halo stars.

These results force us to consider other scenarios that may replicate the observations. In addition to the Aquarius group not being chemically coherent, there is an unusually wide spread in the velocity distribution. Generally a stellar stream is considered kinematically ‘cold’ when its velocity dispersion is $\lesssim 8 \text{ km s}^{-1}$. We find the velocity dispersion from five members to near $\sim 30 \text{ km s}^{-1}$, consistent with the dispersion of 27 km s^{-1} reported by Williams et al. (2011) when all stream members are included. Hypotheses to explain the Aquarius co-moving group must reconcile this wide velocity dispersion.

There are other co-moving groups in the Milky Way that were initially considered as tidal tails from disrupted satellites that are now explainable as signatures of galaxy formation that are not specific accretion events. Like the Aquarius group, the Hercules moving group is significantly offset from the bulk of the observed velocity distribution. Members of the Hercules group exhibit a wide range of metallicities and ages (Bensby et al. 2007; Bovy & Hogg 2010). The observations are well replicated in simulations by stars in the outer disc resonating with the bar in the central region of the Milky Way (Dehnen 2000; Fux 2001), and strong predictions are made for disc velocity distributions that would lend further weight to this hypothesis (Bovy 2010). The Canis Major stellar over-density was also first considered to be an accretion feature from the Canis Major dwarf spheroidal galaxy (Martin et al. 2004). However, Momany et al. (2004) demonstrate the star counts, proper-motions, photometry and kinematics of the ‘accreted feature’ can be easily explained by the warp and flare in the outer thick disc. The Monoceros ring (Newberg et al. 2002; Jurić et al. 2008) is perhaps another example of such an occurrence, as similar features naturally emerge as a consequence of galaxy-satellite interactions (Purcell et al. 2011), which has prompted considerable discussion (Lopez-Corredoira et al. 2012). It is clear that not all significant deviantly kinematic groups are evidence of accretion or tidal tails: in many scenarios a galactic origin is more likely, and simpler.

We hypothesise that the Aquarius group is the result of displaced stars from a perturbation in the thick disc. That is, the stars are galactic in origin but have been displaced by a disc-satellite interaction. Minor mergers can significantly disrupt the host galaxy (Villalobos & Helmi 2008), producing extended spatial and kinematic structure in the process. Minchev et al. (2009) proposed that such a perturbation would cause a galactic ‘ringing’ effect in the neighbourhood surrounding the merger site, analogous to the resulting interference pattern from a stone falling in water and propagating outwards. Stars

move closer together in constructive interference nodes, a signature which is observable in the velocities and orbits of nearby stars. This signature is most prominent in the u - v velocity plane as concentric circles (Gómez et al. 2012a), and dissolves over time (a few Gyr, depending on the mass of the perturber). After the u - v velocity signature dissipates, a clear signature in angular momentum and orbital energy (L_Z, E) persist for long periods following the merger (e.g. see Gómez et al. 2012a).

Through simulations of Milky Way-Sagittarius simulations, Purcell et al. (2011) found that the disc-satellite interactions can explain ringing perturbations within the disc. Additionally, Widrow et al. (2012) and Gómez et al. (2012b) independently observed these phenomena – a ‘wavelike perturbation’, as it was described by Widrow – in the SDSS and SEGUE catalogues. More recently, Gómez et al. (2013) proposed that these patterns were induced by the Sagittarius dSph interacting with the disc. Their simulations reproduce the observed north-south asymmetries and vertical wave-like structure, and show that the amplitude of these oscillations is strongly dependent on galactocentric distance. Combined with the oscillating vertical motions with the u - v velocity pattern, corrugated waves are observed as a result of the interaction.

The stars in these oscillations should exhibit a wide range of ages, metallicities and a large spread in velocity dispersion. Thus, resultant oscillations following a disc-satellite interaction can satisfactorily explain the existence of the Aquarius co-moving group. We do not observe a distinct coherence in the u - v velocity plane in our data, but the angular momentum and orbital energies for Aquarius members qualitatively reproduces the theoretically predicted pattern by Gómez et al. (2012a). The extent and gradient of this L_Z - E signature is dependent on the mass of the perturber, and the time since infall. Although our sample size is minute – and the sample size would still be small even if all Aquarius members had reliable orbits – the fact that we see no u - v velocity coherence is consistent with the observed L_Z - E pattern: signatures in the L_Z - E plane become more extended (Figure 8) over time as the u - v signature dissipates. This is consistent with a disc-satellite interaction occurring in the disc approximately a few Gyr ago.

The Aquarius co-moving group resides at a low latitude ($b \approx -55^\circ$) and with a radial distance of up to $\sim 5 \text{ kpc}$ for some stars, the stars are slightly out of the plane. This is not inconsistent with a disc-satellite interaction. Gómez et al. (2013) find that a significant fraction of the total energy goes into vertical perturbations. While the mean vertical distance $\langle Z \rangle$ in their simulations are near zero, this is an average of disc particles at all plane heights, and the dispersions around $\langle Z \rangle$ are very large (F. Gómez, private communication, 2013). Moreover, Gómez et al. (2013) were only able to reliably track particles up to $|Z| \approx 1.4 \text{ kpc}$ due to a finite number of particles in each cell volume.

If the Aquarius group is a feature of a disc-satellite interaction, the perturber must have a mass on the order of a large globular cluster or a dSph to produce the residual pattern in orbital energy and angular momentum. The Sagittarius dSph galaxy is an obvious candidate, but ω -Centauri is also a possible perturber. We identify C222531-145437 as tidal debris from ω -Centauri, and its

location overlaps with the apocenter of ω -Centauri's orbit. In addition, its velocity matches precisely with simulations of tidal debris by Majewski et al. (2012). Thus, perhaps ω -Centauri disrupted galactic stars as it passed through the plane, adding to any other oscillating modes rippling through the disc, resulting in what we now observe as the Aquarius co-moving group.

5. CONCLUSIONS

We have presented a detailed chemical and dynamical analysis for five members of the recently discovered Aquarius co-moving group from data taken with the MIKE spectrograph on the Magellan Clay telescope. Hereafter we solely refer to the discovery as a co-moving group instead of a stellar stream because we find no evidence that the group is the result of a tidally disrupted globular cluster (or dSph satellite), contrary to the claim by Wylie-de Boer et al. (2012). These conclusions are drawn from a sample size comprising of a third of all the known Aquarius members. The main conclusions are as follows:

- The Aquarius feature is not chemically coherent. A wide spread in metallicities is observed, with $[\text{Fe}/\text{H}]$ ranging from -0.63 to -1.63 dex in just five candidates.
- The co-moving group shows an alpha enhancement of $[\alpha/\text{Fe}] = +0.40$ dex ($+0.38$ if the peculiar star C222531-145437 is excluded), contrary to that typically observed in stars within dSph galaxies.
- Aquarius members are enhanced in $[\text{Na}/\text{Fe}]$ and $[\text{Ni}/\text{Fe}]$ to levels typically observed in either the thick disc or globular clusters. These levels of $[\text{Na}/\text{Fe}]$, $[\text{Ni}/\text{Fe}]$ enhancement are not observed in stars from dSph galaxies either. Thus, on the basis of sodium, nickel, and α -element abundances, it is unlikely the Aquarius co-moving group is the result of a tidally disrupted dSph galaxy.
- We find no evidence for Aquarius group resulting from a disrupted classical globular cluster. No Na-O anti-correlation is observed. Two candidates have slightly enhanced levels of sodium with respect to iron. However, we reiterate that our $[\text{Na}/\text{Fe}]$ abundance ratios appear $+0.10$ dex systematically higher than measurements made by other groups in both our program or standard stars. If the candidates were *known globular cluster members*, they would be classified as belonging to either the primordial component, or at most, the base of the intermediate group.
- We find a positive Mg-Al relationship, also contrary to observations made in globular cluster stars. Given that a Na-O anti-correlation is not evident, it is perhaps unsurprising that no Mg-Al relationship is present since this chemical pattern is less prominent in globular clusters.
- If the Aquarius co-moving group is the result of a disrupted globular cluster, then the large metallicity variation within the stream severely limits the number of possible parent hosts, and both the

extreme and intermediate component of the Na-O anti-correlation have still not been observed.

- One of our candidates, C222531-145437, has chemistry that is clearly distinct from the other Aquarius members. It is enhanced in light elements and shows a strong heavy element enhancement, most notably in barium where $[\text{Ba}/\text{Fe}] = 0.68$ dex. We exclude the possibility that the abundance variations have resulted from an unseen AGB companion through comparisons of expected light and heavy *s*-process yields for AGB stars with a range of stellar masses at the same metallicity as C222531-145437. The position and velocity of C222531-145437 coincides precisely where simulations by Majewski et al. (2012) suggest large amounts of ω -Centauri tidal debris should be found, and its chemistry is precisely consistent with that of RGB stars in the core of ω -Centauri (Marino et al. 2011). The data suggests that C222531-145437 is a rare tidal debris member of the globular cluster ω -Centauri. With a $[\text{Fe}/\text{H}] = -1.22$ dex, it matches the mean metallicity of a known sub-population within ω -Centauri, and removing C222531-145437 from the Aquarius sample does not resolve the aforementioned metallicity spread.
- While no evidence exists for an accreted origin, and the Aquarius members are indistinguishable from thick disc/halo stars, we hypothesise the co-moving group is the result from a disc-satellite interaction. We see no coherent pattern in the $u-v$ plane from Monte-Carlo simulations, but the orbital energies and angular momenta for Aquarius candidates qualitatively reproduces patterns predicted by Gómez et al. (2012a). This is consistent with a minor merger in the Milky Way occurring perhaps up to a few Gyr ago. Given the location and velocity of the Aquarius group, and the identification of C222531-145437 as a disrupted ω -Centauri star, it is plausible that the Milky Way- ω Cen interaction sufficiently perturbed outer disc/halo stars to produce what we now observe as the Aquarius group.

It is clear that not all kinematic substructures are tidal tails of disrupted satellites, and that the structure of the Milky Way is indeed complex. While we find no chemical evidence that the Aquarius group is a tidal tail from a disrupted satellite, we propose the members are galactic in origin, and the co-moving group is a result of a disc-satellite interaction. Thus, while the Aquarius group has not been accreted onto the galaxy, it certainly adds to the rich level of substructure within the Milky Way.

We are indebted to David Nidever and Steven Majewski for kindly replicating a plot from their ω -Centauri simulations (Figure 15 in this text) which helped to place C222531-145437 in context of the cluster's tidal debris. A.R.C. acknowledges the financial support through the Australian Research Council Laureate Fellowship LF0992131, and from the Australian Prime Minister's Endeavour Award Research Fellowship which

has facilitated his research at MIT. This publication makes use of data products from the Two Micron All Sky Survey, which is a joint project of the University of Massachusetts and the Infrared Processing and Analysis

Center/California Institute of Technology, funded by the National Aeronautics and Space Administration and the National Science Foundation.

REFERENCES

- Allende Prieto, C., Lambert, D. L., & Asplund, M. 2001, ApJ, 556, L63
- Alonso, A., Arribas, S., & Martínez-Roger, C. 1999, A&AS, 140, 261
- Aoki, W., et al. 2007, ApJ, 660, 747
- Arnett, W. D., & Truran, J. W. 1969, ApJ, 157, 339
- Arnould, M., Goriely, S., & Jorissen, A. 1999, A&A, 347, 572
- Asplund, M., & García Pérez, A. E. 2001, A&A, 372, 601
- Asplund, M., Grevesse, N., Sauval, A. J., & Scott, P. 2009, ARA&A, 47, 481
- Barber, C., Dobkin, D., & Huhdanpaa, H. 1996, ACM Transactions on Mathematical Software (TOMS), 22, 469
- Baumueller, D., & Gehren, T. 1997, A&A, 325, 1088
- Bekki, K., & Freeman, K. C. 2003, MNRAS, 346, L11
- Belokurov, V., et al. 2007, ApJ, 658, 337
- Bensby, T., Oey, M. S., Feltzing, S., & Gustafsson, B. 2007, ApJ, 655, L89
- Bernstein, R., Shectman, S. A., Gunnels, S. M., Mochnicki, S., & Athey, A. E. 2003, in Society of Photo-Optical Instrumentation Engineers (SPIE) Conference Series, Vol. 4841, Society of Photo-Optical Instrumentation Engineers (SPIE) Conference Series, ed. M. Iye & A. F. M. Moorwood, 1694–1704
- Bovy, J. 2010, ApJ, 725, 1676
- Bovy, J., & Hogg, D. W. 2010, ApJ, 717, 617
- Breddels, M. A., et al. 2010, A&A, 511, A90
- Burnett, B., & Binney, J. 2010, MNRAS, 407, 339
- Burris, D. L., Pilachowski, C. A., Armandroff, T. E., Sneden, C., Cowan, J. J., & Roe, H. 2000, ApJ, 544, 302
- Carretta, E., et al. 2009, A&A, 505, 117
- Casagrande, L., Ramírez, I., Meléndez, J., Bessell, M., & Asplund, M. 2010, A&A, 512, A54
- Castelli, F., & Kurucz, R. L. 2003, in IAU Symposium, Vol. 210, Modelling of Stellar Atmospheres, ed. N. Piskunov, W. W. Weiss, & D. F. Gray, 20P
- Cayrel, R., et al. 2004, A&A, 416, 1117
- Da Costa, G. S., & Coleman, M. G. 2008, AJ, 136, 506
- De Silva, G. M., D’Orazi, V., Melo, C., Torres, C. A. O., Gieles, M., Quast, G. R., & Sterzik, M. 2013, ArXiv e-prints
- Dehnen, W. 2000, AJ, 119, 800
- Dinescu, D. I. 2002, in Astronomical Society of the Pacific Conference Series, Vol. 265, Omega Centauri, A Unique Window into Astrophysics, ed. F. van Leeuwen, J. D. Hughes, & G. Piotto, 365
- Dinescu, D. I., Girard, T. M., & van Altena, W. F. 1999, AJ, 117, 1792
- Dotter, A., Chaboyer, B., Jevremović, D., Kostov, V., Baron, E., & Ferguson, J. W. 2008, ApJS, 178, 89
- Drake, A. J., et al. 2013, ArXiv e-prints
- Francois, P., Spite, M., & Spite, F. 1988, A&A, 191, 267
- Frebel, A., Casey, A. R., Jacobson, H. R., & Yu, Q. 2013, ArXiv e-prints
- Freeman, K., & Bland-Hawthorn, J. 2002, ARA&A, 40, 487
- Fulbright, J. P. 2000, AJ, 120, 1841
- Fux, R. 2001, A&A, 373, 511
- García Pérez, A. E., Asplund, M., Primas, F., Nissen, P. E., & Gustafsson, B. 2006, A&A, 451, 621
- Gómez, F. A., Minchev, I., O’Shea, B. W., Beers, T. C., Bullock, J. S., & Purcell, C. W. 2013, MNRAS, 429, 159
- Gómez, F. A., Minchev, I., Villalobos, Á., O’Shea, B. W., & Williams, M. E. K. 2012a, MNRAS, 419, 2163
- Gómez, F. A., et al. 2012b, MNRAS, 423, 3727
- Gratton, R. G., & Sneden, C. 1991, A&A, 241, 501
- Gratton, R. G., Sneden, C., Carretta, E., & Bragaglia, A. 2000, A&A, 354, 169
- Grevesse, N., & Sauval, A. J. 1998, Space Sci. Rev., 85, 161
- Hansen, C. J., Bergemann, M., Cescutti, G., François, P., Arcones, A., Karakas, A. I., Lind, K., & Chiappini, C. 2013, A&A, 551, A57
- Helmi, A., & White, S. D. M. 1999, MNRAS, 307, 495
- Hinkle, K., Wallace, L., Livingston, W., Ayres, T., Harmer, D., & Valenti, J. 2003, in The Future of Cool-Star Astrophysics: 12th Cambridge Workshop on Cool Stars, Stellar Systems, and the Sun, ed. A. Brown, G. M. Harper, & T. R. Ayres, Vol. 12, 851–856
- Jurić, M., et al. 2008, ApJ, 673, 864
- Lawler, J. E., Bonvallet, G., & Sneden, C. 2001, ApJ, 556, 452
- Lopez-Corredoira, M., Moitinho, A., Zaggia, S., Momany, Y., Carraro, G., Hammersley, P. L., Cabrera-Lavers, A., & Vazquez, R. A. 2012, ArXiv e-prints
- Majewski, S. R., Nidever, D. L., Smith, V. V., Damke, G. J., Kunkel, W. E., Patterson, R. J., Bizyaev, D., & García Pérez, A. E. 2012, ApJ, 747, L37
- Marino, A. F., et al. 2011, A&A, 532, A8
- Martin, N. F., Ibata, R. A., Bellazzini, M., Irwin, M. J., Lewis, G. F., & Dehnen, W. 2004, MNRAS, 348, 12
- Minchev, I., Quillen, A. C., Williams, M., Freeman, K. C., Nordhaus, J., Siebert, A., & Bienaymé, O. 2009, MNRAS, 396, L56
- Miyamoto, M., & Nagai, R. 1975, PASJ, 27, 533
- Momany, Y., Zaggia, S. R., Bonifacio, P., Piotto, G., De Angeli, F., Bedin, L. R., & Carraro, G. 2004, A&A, 421, L29
- Munari, U., Sordo, R., Castelli, F., & Zwitter, T. 2005, A&A, 442, 1127
- Munari, U., & Zwitter, T. 1997, A&A, 318, 269
- Nataf, D. M., et al. 2012, ArXiv e-prints
- Navarro, J. F., Frenk, C. S., & White, S. D. M. 1997, ApJ, 490, 493
- Newberg, H. J., et al. 2002, ApJ, 569, 245
- Nissen, P. E., Chen, Y. Q., Schuster, W. J., & Zhao, G. 2000, A&A, 353, 722
- Nissen, P. E., & Schuster, W. J. 1997, A&A, 326, 751
- . 2010, A&A, 511, L10
- . 2011, A&A, 530, A15
- Nordström, B., et al. 2004, A&A, 418, 989
- Norris, J. E., & Da Costa, G. S. 1995, ApJ, 441, L81
- Norris, J. E., Ryan, S. G., & Beers, T. C. 1996, ApJS, 107, 391
- . 2001, ApJ, 561, 1034
- Peek, J. E. G., & Graves, G. J. 2010, ApJ, 719, 415
- Plez, B., Masseron, T., & Van Eck, S. 2008, in Cool Stars, Stellar Systems and the Sun, ASP Conference Series
- Purcell, C. W., Bullock, J. S., Tollerud, E. J., Rocha, M., & Chakrabarti, S. 2011, Nature, 477, 301
- Reddy, B. E., Lambert, D. L., & Allende Prieto, C. 2006, MNRAS, 367, 1329
- Reddy, B. E., Tomkin, J., Lambert, D. L., & Allende Prieto, C. 2003, MNRAS, 340, 304
- Robin, A. C., Reylé, C., Derrière, S., & Picaud, S. 2003, A&A, 409, 523
- Roederer, I. U., Sneden, C., Thompson, I. B., Preston, G. W., & Shectman, S. A. 2010, ApJ, 711, 573
- Schlegel, D. J., Finkbeiner, D. P., & Davis, M. 1998, ApJ, 500, 525
- Schönrich, R. 2012, MNRAS, 427, 274
- Sharma, S., Bland-Hawthorn, J., Johnston, K. V., & Binney, J. 2011, ApJ, 730, 3
- Shetrone, M. D. 1996, AJ, 112, 1517
- Siebert, A., et al. 2011, AJ, 141, 187
- Skrutskie, M. F., et al. 2006, AJ, 131, 1163
- Smith, V. V., Suntzeff, N. B., Cunha, K., Gallino, R., Busso, M., Lambert, D. L., & Straniero, O. 2000, AJ, 119, 1239
- Sneden, C. A. 1973, PhD thesis, The University of Texas at Austin.
- Sobeck, J. S., et al. 2011, AJ, 141, 175
- Steinmetz, M., et al. 2006, AJ, 132, 1645
- Travaglio, C., Gallino, R., Arnone, E., Cowan, J., Jordan, F., & Sneden, C. 2004, ApJ, 601, 864
- Tsuchiya, T., Dinescu, D. I., & Korchagin, V. I. 2003, ApJ, 589, L29

- Tsuchiya, T., Korochagin, V. I., & Dinescu, D. I. 2004, MNRAS, 350, 1141
- Villalobos, Á., & Helmi, A. 2008, MNRAS, 391, 1806
- Widrow, L. M., Gardner, S., Yanny, B., Dodelson, S., & Chen, H.-Y. 2012, ApJ, 750, L41
- Williams, M. E. K., et al. 2011, ApJ, 728, 102
- Woosley, S. E., & Weaver, T. A. 1995, ApJS, 101, 181
- Wylie-de Boer, E., Freeman, K., Williams, M., Steinmetz, M., Munari, U., & Keller, S. 2012, ApJ, 755, 35
- Yong, D., Carney, B. W., & Teixera de Almeida, M. L. 2005, AJ, 130, 597
- Zwitter, T., et al. 2008, AJ, 136, 421
- . 2010, A&A, 522, A54